



Semi-automatic vessel detection for challenging cases of peripheral arterial disease

Gabriel Mistelbauer^{a,*}, Anca Morar^{b,**}, Rüdiger Schernthaner^c, Andreas Strassl^d, Dominik Fleischmann^e, Florica Moldoveanu^b, M. Eduard Gröller^{f,g}

^a Department of Simulation and Graphics, Otto-von-Guericke University Magdeburg, Germany

^b Department of Computer Science, University Politehnica of Bucharest, Romania

^c Department of Radiology, Hospital Landstrasse, Vienna, Austria

^d Department of Biomedical Imaging and Image-guided Therapy, Medical University of Vienna, Austria

^e Department of Radiology, Stanford University School of Medicine, Stanford, USA

^f Institute of Visual Computing and Human-Centered Technology, TU Wien, Austria

^g VRVis Research Center, Austria

ARTICLE INFO

Keywords:

Blood vessel segmentation
Vessel tracking
Active contours without edges
Angiography

ABSTRACT

Objectives: Manual or semi-automated segmentation of the lower extremity arterial tree in patients with Peripheral arterial disease (PAD) remains a notoriously difficult and time-consuming task. The complex manifestations of the disease, including discontinuities of the vascular flow channels, the presence of calcified atherosclerotic plaque in close vicinity to adjacent bone, and the presence of metal or other imaging artifacts currently preclude fully automated vessel identification. New machine learning techniques may alleviate this challenge, but require large and reasonably well segmented training data.

Methods: We propose a novel semi-automatic vessel tracking approach for peripheral arteries to facilitate and accelerate the creation of annotated training data by expert cardiovascular radiologists or technologists, while limiting the number of necessary manual interactions, and reducing processing time. After automatically classifying blood vessels, bones, and other tissue, the relevant vessels are tracked and organized in a tree-like structure for further visualization.

Results: We conducted a pilot (N = 9) and a clinical study (N = 24) in which we assess the accuracy and required time for our approach to achieve sufficient quality for clinical application, with our current clinically established workflow as the standard of reference. Our approach enabled expert physicians to readily identify all clinically relevant lower extremity arteries, even in problematic cases, with an average sensitivity of 92.9%, and an average specificity and overall accuracy of 99.9%.

Conclusions: Compared to the clinical workflow in our collaborating hospitals (28:40 ± 7:45 [mm:ss]), our approach (17:24 ± 6:44 [mm:ss]) is on average 11:16 [mm:ss] (39%) faster.

1. Introduction

Peripheral arterial disease (PAD) is the clinical manifestation of diminished blood flow to the legs due to atherosclerotic plaque obstructing the branches of the lower extremity arterial tree. PAD is common in the developed world, with > 20% of patients older than 80 years being affected [48]. Patients either experience leg pain when

walking (intermittent claudication), or may present with rest pain or tissue loss (critical limb ischemia), requiring surgical (e.g. bypass grafting) or endovascular (percutaneous transluminal angioplasty (PTA)) revascularization. Imaging is required before revascularization to confirm the presence and extent of disease, and to accurately localize the culprit lesions within the lower extremity arterial tree.

Computed tomography angiography (CTA) has been routinely used

* Corresponding author.

** Corresponding author.

E-mail addresses: gmistelbauer@isg.cs.uni-magdeburg.de (G. Mistelbauer), anca.morar@cs.pub.ro (A. Morar), ruediger.schernthaner@gesundheitsverbund.at (R. Schernthaner), andreas.strassl@meduniwien.ac.at (A. Strassl), d.fleischmann@stanford.edu (D. Fleischmann), florica.moldoveanu@cs.pub.ro (F. Moldoveanu), groeller@cg.tuwien.ac.at (M.E. Gröller).

<https://doi.org/10.1016/j.combiomed.2021.104344>

Received 9 December 2020; Received in revised form 26 February 2021; Accepted 12 March 2021

Available online 18 March 2021

0010-4825/© 2021 Elsevier Ltd. All rights reserved.

for pre-interventional diagnosis and treatment planning in patients with PAD for more than two decades [1,10,35,47,54]. In spite of many technical advances in imaging and post-processing technology over the last 20 years, accurate visualization and mapping of obstructive lesions within the large peripheral arterial tree remains a considerable challenge in clinical practice: The extraction of arterial centerlines—a prerequisite to the generation of curved planar reformations (CPRs)—requires considerable user interaction and is one of the most time-consuming post-processing tasks performed in a clinical ‘3D-Lab’. Many traditional image processing approaches [6,26,36] work very well in non-diseased vessels, but do not provide satisfying results in difficult PAD cases. These are usually characterized by:

- an unpredictable lesion location,
- the eccentricity of the narrowed flow channels within an arterial cross-section,
- the possibility of complete interruption of the arterial flow channels over variable lengths,
- the presence of atherosclerotic calcifications which obscure the flow lumen and have computed tomography (CT) attenuation values similar to adjacent bones, and, finally,
- the presence of imaging artifacts, such as noise, motion, and metal artifacts from, e.g. joint implants.

Neural networks aim to reduce manual efforts from users once they are trained with sufficiently well segmented data sets [66]. There is a wealth of scientific work on machine learning models for vascular tracking and segmentation, but the majority is concerned with retinal [49], pulmonary [34,59], carotid [40,45,63], adrenal [66] and coronary vessels [28,61,68] or other internal structures [57]. There are only a few solutions for peripheral CTA vessel segmentation, as noted by Moccia et al. [29]. The lack of scientific research on machine learning for peripheral vessel tracking may be caused by the shortage of accurately labeled, i.e., ground truth, training data.

Our current clinical semi-automated vessel segmentation approach [17] is well tested and robust, but also time-consuming (about 30 min per case) and requires a considerable amount of user interaction to overcome the subsequent specific **challenges** encountered with PAD:

- vessels touching bone,
- discontinuities (e.g. non-uniform opacified vessels),
- bone-like regions (e.g. calcifications and stents), and
- metal hardware artifacts (e.g. hip joint implants).

In order to leverage the possibilities of machine learning, we designed an improved approach that replaces some parts of the current workflow and generates ground truth data by expert users much faster. To the best of our knowledge, there is no semi-automated or automated workflow that captures and identifies the relevant arteries for PAD, which is deliberately designed to handle difficult cases. Specifically, we provide a comprehensive description of these cases and propose an approach that:

- solves the above-mentioned challenges with PAD,
- is faster than our current clinical approach,
- provides similar accuracy and robustness, and
- requires significantly less user interaction.

This would not only make clinical use more efficient, but also help us to generate labeled ground truth data for a total of almost 7000 data sets that we collected over the past years.

2. Related work

Our approach concerns bone removal, blood vessel segmentation, and tracking. The subsequent paragraphs describe the most relevant work in these fields. In the last paragraph, we also relate our work to

machine learning.

2.1. Bone removal

To provide an unobstructed view of blood vessels, bones have to be removed beforehand, because the intensity values of bones are usually higher or similar to blood vessels in CT and CTA data, respectively. This can either be accomplished with a simple threshold, bone-to-bone elimination between two series of images [9], registration of two data sets with or without contrast agent [25], or simultaneous label fusion using atlases [64]. Bone removal is particularly useful for maximum intensity projection (MIP), a commonly used visualization technique that allows experts to analyze structures with the highest intensity values in a data set.

2.2. Vessel segmentation

Many vessel segmentation techniques enhance the vessels first, such as applying a Gabor or Frangi filter [52], doing a gradient analysis [32], or performing anisotropic filtering [4]. Other approaches include fuzzy connectedness [58], morphology-based segmentation and intensity probability distributions [11], graph-cuts [11,41], particle filtering [46], and seeded region growing [19,53].

Kirbas and Quek [20] provide a comprehensive review of several vessel segmentation approaches. Cetin et al. [7] present a segmentation algorithm that is based on a second order tensor model, inspired from diffusion tensor image modeling. Hong et al. [14] introduce a localized hybrid level-set method for 3D vessel segmentation, integrating both local region and boundary information. Multi-scale vessel-specific features (Frobenius norm of the Hessian Eigenvalues, LoG, oriented second derivative, etc.) can be used for segmentation of vessels in confocal images [18]. Vascular structures may be described as tubular objects in medical 3D data sets and their centerlines are well defined and can be extracted [2,3]. Similarly, a tube detection filter for 3D centerline extraction based on multi-scale medialness can be used [38]. Olabarriaga et al. [37] propose a semi-automatic centerline extraction technique for coronary arteries in CT images, using a local filter and a minimum-cost path algorithm. Manniesing et al. [27] propose a 3D vessel segmentation and centerline extraction that is based on constrained surface evolution. They analyze the skeleton during evolution and impose a shape constraint on the topology. Lidayova et al. [23] present a 4-tiered algorithm that recognizes centerlines of diseased peripheral arteries. Two tiers deal with the detection of healthy arteries of different sizes, while the other two are specialized on calcifications and occlusions.

2.3. Vessel tracking

Vessel segmentation assigns pixels or voxels to certain tissue classes, e.g., vessel, bone, or other tissue. Tracking goes one step further by specifying the relations between the elements of the vessel class, organizing the vasculature into a graph or tree structure. Multiple hypotheses tracking is used in several works [12,43], but designed for either small vessels [12], or only validated on coronary arteries and airway trees [43]. A directional fast marching algorithm, improved with a multi-model strategy, is used by Jia and Zhuang [16] to extract coronary centerlines. Grölsün et al. [13] determine a geodesic path between tree shapes using Dijkstra’s algorithm and propose a method that propagates labels from an atlas-based coronary arterial tree model to unlabeled coronary centerlines. Zhao et al. [65] merge discontinuities in segmented vessel trees by employing skeletonization and a nonlinear least square fitting. Shim et al. [46] perform tracking by modeling a vessel segment as an ellipse moving in 3D space.

Other approaches represent vessel trajectories as 4D curves, where the first three dimensions are used for the spatial coordinates, and the fourth dimension is the radius [22,30]. Shahzad et al. [44] present a

fully automated algorithm for vessel segmentation and tracking for whole body magnetic resonance angiography (MRA) data sets, where tree branches are labeled with a combination of graph-based and atlas-based approaches. Challenging cases are, however, not discussed. A single seed point is required by the approach of Borges Oliveira et al. [5] to track the entire vascular networks of the coronary, carotid, and pulmonary arteries. Major et al. [24] describe an automatic method for detecting the main arteries of three body regions by identifying seed points within the aorta, carotid arteries, and iliac arteries. Novikov et al. [36] extended this approach with a fully automated framework that detects body parts, extracts vessel centerlines, and employs anatomy-driven connection rules to track the vascular tree. Arteries below the knee—a key clinical requirement for the assessment of PADs—are not covered. Moriconi et al. [33] track vessel trees by solving a connectivity-optimized anisotropic level-set over a voxel-wise tensor field that represents the orientation of the vasculature. Their method was evaluated with different imaging modalities, including CTA, but only at the cerebral level. The approach of Hu et al. [15] can detect vessels even in difficult cases such as stenoses, calcifications, and stents, by using training samples on multiple scales. The method was evaluated on synthetic vascular data sets, carotid and aortoiliac arteries. Although they deal with several pathologies, other difficult cases such as vascular discontinuities, which are common in PADs, are not discussed.

2.4. Machine learning (ML)

In this paragraph we discuss several ML-based approaches in the area of vessel segmentation and tracking. Wu et al. [62] use a convolutional neural network (CNN) to learn the appearance and features of the retinal vasculature. A nearest neighbor search based on a principal component analysis (PCA) is used to estimate the local structure distribution and to extract the vessel tree. A stacked fully convolutional network segments pulmonary vessels and is followed by an orientation-based region growing to track the vasculature [59]. Nardelli et al. [34] use a 3D CNN to obtain a first classification of vessels and refine the results with graph-cuts. Shi et al. [45] perform slice-based segmentation of 3D magnetic resonance brain images with a U-Net-like fully convolutional network by hierarchical extraction of low- and high-order convolutional features. Another method based on U-Nets is proposed by Xie et al. [63], which uses single and multi-path convolutional networks to identify the carotid vessel lumen in ultrasound images. Sanches et al. [40] introduce a cerebrovascular vessel segmentation framework, entitled Uception, inspired by U-Net 3D and by Inception modules. Mirunalini et al. [28] combine a CNN with recurrent neural networks to identify the presence of coronary arteries in 2D slices from CTA data sets. Next, they apply a U-Net model to segment vessels which are reconstructed into 3D coronary arteries using MIP. Another multi-task recurrent CNN is applied by Zreik et al. [68] on multi-planar reformatted images of coronary arteries to detect and classify artery plaque and stenosis. They also analyze coronary arteries in cardiac CTA to detect patients requiring invasive coronary angiography [67]. Wolterink et al. [61] extract centerlines with a 3D dilated CNN trained to predict the most likely direction and radius of an artery at a given point in a cardiac CTA data set, based on a local image patch. Tetteh et al. [55] introduced Deep-VesselNet, a tool that segments vessels, predicts centerlines, and detects bifurcations in 3D angiographic volumes. Their method is validated on MRA data sets of the human brain and X-ray tomographic microscopy scans of rat brains. Transfer learning was used to segment the vasculature of mouse brains with high accuracy [56].

The current development and early success of ML algorithms applied to vascular imaging data address the limitations of clinical visualization of diseased arteries in patients with PAD. Due to the specific anatomic distribution of the disease within and across patients, the wide variability of atherosclerotic plaque composition, the extent and location relative to the residual or completely occluded flow channels, we foresee the need for a large amount of ground truth data to be required for the

development, training, and validation of any new algorithm for clinical PAD imaging and visualization.

The purpose of this work is to improve an existing, clinically used semi-automated bone segmentation and vessel tracking algorithm for the assessment of PAD. In addition, our approach accelerates the generation of expert derived ground truth data so that new ML algorithms can be trained and tested in the future.

3. Methods

Accurate assessment of vascular lesions, such as in PAD, requires the

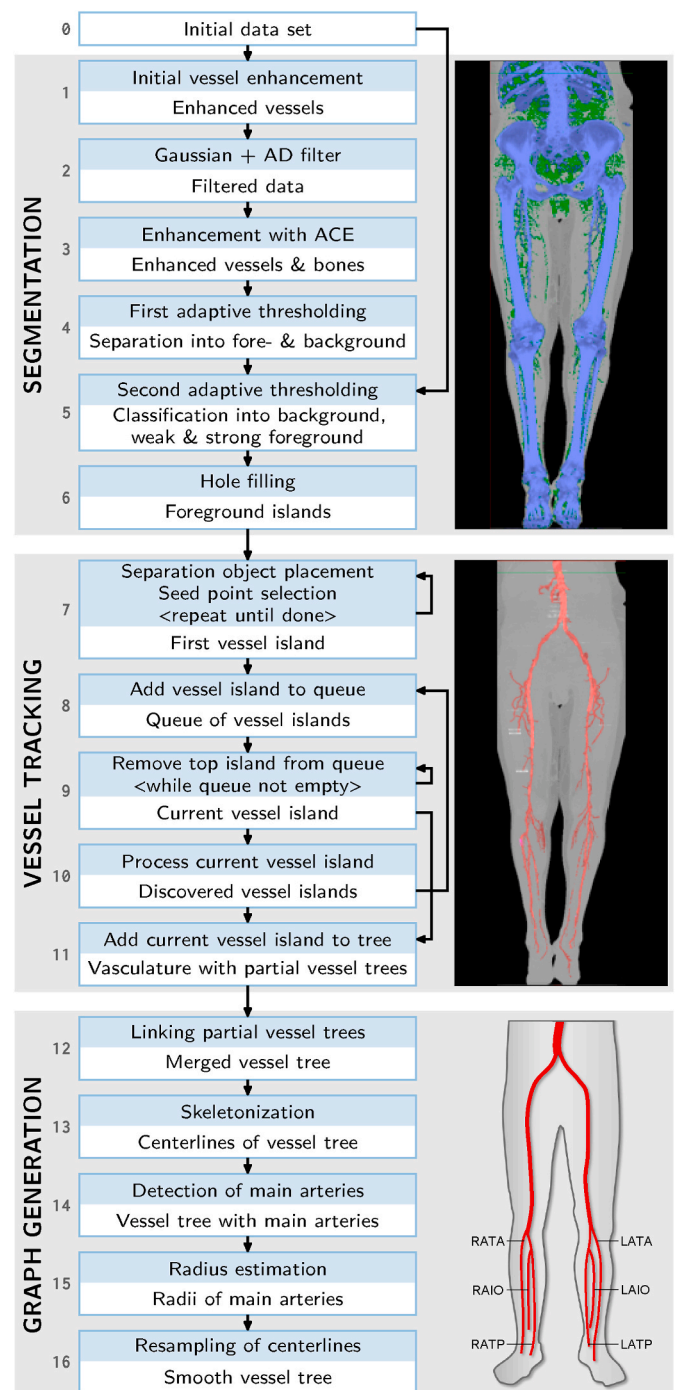


Fig. 1. Workflow of our proposed approach. A detailed description of Step 10 is given in Fig. 3 and Fig. 4.

extraction of arterial centerlines. Furthermore, representing the vascular system as a tree of vessel centerlines forms the basis for diagnostic visualization techniques, such as CPR and multipath curved planar reformation (mpCPR) [39]. However, a simple segmentation or classification of bones, vessels, or other tissues is not sufficient. This is even more constrained by the fact that not all blood vessels are diagnostically relevant and, by the human uniqueness, leading to highly varying vascular systems between patients. A vessel detection approach must account for all these critical aspects and, additionally, consider vessel occlusions, eccentricities of stenoses, calcifications, stents or even artificial joints that are increasingly occurring.

The evaluation of patients with PAD requires the assessment of the entire lower extremity arterial tree. This includes the abdominal aorta as its root, the bilateral common and external iliac arteries, the bilateral common and superficial femoral arteries, the bilateral popliteal arteries, and finally three below-knee arteries for each leg (see bottom-right illustration of Fig. 1): right/left arteria tibialis anterior (ATA), right/left arteria interossea (AIO), and the right/left arteria tibialis posterior (ATP). To segment these vessels, we extend the approach proposed by Morar et al. [31], which is based on active contours without edges (ACE)

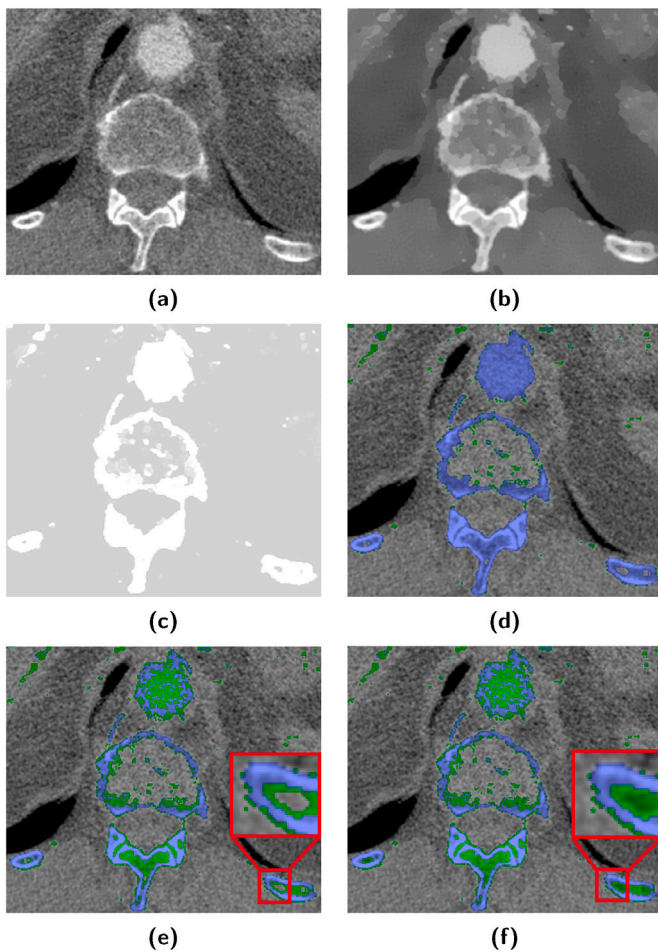


Fig. 2. Segmentation stage. (a) shows an initial image of the data set. (b) presents the image after initial vessel enhancement, followed by smoothing with a Gaussian filter and an anisotropic diffusion filter. (c) shows the enhancement with ACE. (d) demonstrates the output of the first adaptive threshold, differentiating between foreground (blue) and background voxels. (e) shows the result of the first and second adaptive threshold, with weak foreground voxels in green and strong ones in blue. (f) displays the creation of foreground islands with the result of the hole filling step. (For interpretation of the references to colour in this figure legend, the reader is referred to the web version of this article.)

[8]. The workflow of our approach is outlined in Fig. 1 and, subsequently, all steps are explained in detail.

3.1. Segmentation

During CTA, iodinated contrast medium is injected intravenously to opacify the blood flowing in the vascular system. This leads to substantially higher CT attenuation values (Hounsfield units) of blood vessels compared to soft tissues (see Fig. 2a). However, strong vascular opacification often reduces the ability to delineate borders between vessel and bone tissue, which is naturally high in attenuation due to its calcium content. To address this problem, we map all intensity values, slice-by-slice, to a vessel probability between zero and one (see Fig. 1, Step 1) [50]. We then smooth this probability data set with a Gaussian filter followed by a nonlinear anisotropic diffusion filter (see Fig. 2b, Step 2) [51,60]. The former filter removes very small discontinuities within the structures of the scanned body, especially near tissue boundaries. The latter filter smooths the CTA data set without blurring the edges to avoid connecting different foreground structures that are close together, such as the aorta next to the spine. Subsequently, vessels and bones are enhanced using the approach proposed by Morar et al. [31] (Step 3). This results in an enhanced data set \mathcal{E} with intensity values $I_{\mathcal{E}}(\mathbf{v}) \in [0, 1]$ at voxel \mathbf{v} (see Fig. 2c).

The first adaptive threshold (see Fig. 2d, Step 4) is applied to the enhanced data set \mathcal{E} and leads to a clear delineation between background (other tissue, mask value 0) and foreground (vessel and bone tissue, mask value 1), based on abrupt intensity changes at the borders. The resulting mask value $K_1(\mathbf{v})$ of the first adaptive threshold is defined as follows:

$$K_1(\mathbf{v}) = \begin{cases} 0 & \text{if } T_1 > I_{\mathcal{E}}(\mathbf{v}) \\ 0 & \text{if } (T_1 \leq I_{\mathcal{E}}(\mathbf{v}) \leq T_2) \wedge (I_{\mathcal{E}}(\mathbf{v}) < \bar{I}_{\mathcal{E}}(N) \cdot F_1) \\ 1 & \text{if } (T_1 \leq I_{\mathcal{E}}(\mathbf{v}) \leq T_2) \wedge (I_{\mathcal{E}}(\mathbf{v}) \geq \bar{I}_{\mathcal{E}}(N) \cdot F_1) \\ 1 & \text{if } T_2 < I_{\mathcal{E}}(\mathbf{v}) \end{cases}, \quad (1)$$

where $I_{\mathcal{E}}(\mathbf{v})$ is the intensity value at voxel \mathbf{v} in the enhanced data set \mathcal{E} , and $T_1 = 0.38$ and $T_2 = 0.57$ are two empirically determined threshold values. $\bar{I}_{\mathcal{E}}(N)$ is the average intensity within a neighboring window N (with a radius of 10 pixels in the proximal upper half of the data set and 5 pixels in the distal lower half), and F_1 is a fixed parameter with a value slightly larger than 1 (in our experiments, $F_1 \in [1.03, 1.05]$). By multiplying $\bar{I}_{\mathcal{E}}(N)$ with F_1 , we ensure that only a few voxels with values between T_1 and T_2 are set to one. The first adaptive threshold distinguishes well between foreground (1) and background (0), but not between distinct elements of the foreground. If bone and vessel objects are very close to each other, there is a high probability that they will be considered as belonging to a single object. This drawback is addressed in the subsequent steps.

The second adaptive threshold (see Fig. 2e, Step 5) discriminates between different foreground objects. It uses the intensity values (Hounsfield units) of the initial CTA data set, and is defined as follows:

$$K_2(\mathbf{v}) = \begin{cases} 0 & \text{if } I(\mathbf{v}) < \bar{I}(N) \cdot F_2, \\ 1 & \text{if } I(\mathbf{v}) \geq \bar{I}(N) \cdot F_2, \end{cases} \quad (2)$$

where F_2 is a fixed parameter with a value slightly larger than 1 (in our experiments, $F_2 = 1.05$).

Combining the mask values of both adaptive thresholds, the slice's voxels are classified into background, weak foreground, and strong foreground as follows:

$$\text{class}(\mathbf{v}) = \begin{cases} \text{background} & \text{if } K_1(\mathbf{v}) = 0, \\ \text{weak foreground} & \text{if } K_1(\mathbf{v}) = 1 \wedge K_2(\mathbf{v}) = 0, \\ \text{strong foreground} & \text{if } K_1(\mathbf{v}) = 1 \wedge K_2(\mathbf{v}) = 1. \end{cases} \quad (3)$$

The background is referred to as *other tissue* and the foreground (weak

and strong) as *bone + vessel*.

Distinguishing between weak and strong foreground voxels extends the approach of Morar et al. [31], which was initially applied only to bone segmentation. The reason for this is to correctly handle vessels that are smaller than bone and have lower intensity values. Strong voxels have a high probability of belonging to the foreground, whereas weak ones either belong to the foreground, or were wrongly labeled as such, and should belong to the background instead. Voxels that were incorrectly labeled as weak are removed during the vessel tracking. Depending on the transverse slice location within the data set, i.e., proximal (in the upper half of the data set) or distal (in the lower half), as well as on the intensity value, a voxel is either assigned to the strong or weak foreground class. The size of proximal blood vessels is comparable with that of bones and their intensity values allow for a clear separation between foreground and background, and between distinct foreground elements. Vessel voxels in the proximal region are labeled as strong voxels, while voxels belonging to the border between vessels and bones are labeled as weak, or background. Conversely, distal blood vessels are very small and characterized by much lower intensity values than bone. This leads to an unclear delineation of vessel voxels from background or bone. In such situations, vessel voxels are usually labeled as weak foreground.

Subsequently (Step 6), a set of connected *bone + vessel* voxels defines a *foreground island*. All background voxels inside a foreground island are labeled as weak foreground. This ensures that there are no holes inside bone or vessel tissue. After the segmentation stage, every voxel of the input data set is classified as background, weak foreground, or strong foreground. Fig. 2 presents the output of each of these steps.

3.2. Vessel tracking

Vessel tracking is initiated by a user-specified seed point within the *vessel + bone* class, preferably a strong voxel. This seed point is labeled as belonging to *vessel* tissue. When choosing a seed point, large vessels (main arteries) should be preferred. Also, vessel tissue in the upper half of the data set (closer to the patient's head) is a better choice than tissue closer to the patient's legs. Once a seed point has been chosen, the *vessel* label is propagated inside the slice (transverse section) to neighboring voxels that belong to the same class.

A set of connected foreground voxels within one slice defines a *foreground island*. Whenever a foreground island is included into the vessel tree, it is marked as *vessel island*. The first vessel island that contains the seed point is called *seed island*. Once such an island has been found, the algorithm searches its neighborhood within adjacent slices for strong or weak foreground voxels that do not already belong to the vascular tree. Such neighboring voxels define a *candidate island*.

Let \mathcal{I}_V^z be the current vessel island on slice z and $\mathcal{I}_C^{z\pm 1}$ the candidate island on an adjacent slice (i.e., $z \pm 1$). We determine if their sizes differ substantially as follows

$$\Delta S = \begin{cases} \neg\text{substantial} & \text{if } (\delta \leq T_1^S) \wedge (|\mathcal{I}_V^z| < T_1^S), \\ \text{substantial} & \text{if } (\delta > T_1^S) \wedge (|\mathcal{I}_V^z| < T_1^S), \\ \neg\text{substantial} & \text{if } (\delta \leq T_2^S) \wedge (T_1^S \leq |\mathcal{I}_V^z| \leq T_3^S), \\ \text{substantial} & \text{if } (\delta > T_2^S) \wedge (T_1^S \leq |\mathcal{I}_V^z| \leq T_3^S), \\ \neg\text{substantial} & \text{if } (\delta \leq T_3^S) \wedge (|\mathcal{I}_V^z| > T_3^S), \\ \text{substantial} & \text{if } (\delta > T_3^S) \wedge (|\mathcal{I}_V^z| > T_3^S), \end{cases} \quad (4)$$

$$\delta = |\mathcal{I}_C^{z\pm 1}| - |\mathcal{I}_V^z|, \quad (5)$$

where the size of a vessel island \mathcal{I} is defined as the number of contained voxels, denoted by $|\mathcal{I}|$. The size threshold values T_1^S , T_2^S and T_3^S were

empirically determined and depend on the axial slice resolution (X, Y) of the CT data set ($T_1^S = 38 \cdot 10^{-5} \cdot X \cdot Y$, $T_2^S = 2 \cdot T_1^S$, $T_3^S = 5 \cdot T_1^S$). For a typical data set with $X = Y = 512$, this would lead to $T_1^S \approx 100$, $T_2^S \approx 200$, and $T_3^S \approx 500$. The size difference ΔS is always not substantial if the candidate is smaller than the current vessel island, i.e., $\delta < 0$. If the two islands do not substantially differ in size and the number of adjacent voxel pairs $\mathbf{P}(x, y, z)$ and $\mathbf{Q}(x, y, z \pm 1)$ with $\mathbf{P} \in \mathcal{I}_V^z$ and $\mathbf{Q} \in \mathcal{I}_C^{z\pm 1}$ is greater than $\min(|\mathcal{I}_V^z|, |\mathcal{I}_C^{z\pm 1}|)/2$, the candidate island $\mathcal{I}_C^{z\pm 1}$ is labeled as vessel island. If the candidate island $\mathcal{I}_C^{z\pm 1}$ is labeled as vessel island, i.e., belongs to the vessel tree, it is inserted into a queue q_{vi} . In the next step, the first element is dequeued and considered as the new current vessel island \mathcal{I}_V^z (Step 9). Its candidate islands are processed next and inserted into q_{vi} , if they are regarded as being part of the vessel tree as well.

Usually, the current vessel island has only two neighboring islands, one on the upper adjacent slice, and the other one on the lower adjacent slice. One of these neighboring islands, undoubtedly, already belongs to the vessel tree, since it led to the discovery of the current vessel island. This leaves just a single candidate island for the current vessel island, unless there is a case of vessel branching or the current island is a seed one. The tracking stage continues until there are no more elements in q_{vi} .

Whenever blood vessels are tracked, starting from a seed point, a *partial vessel tree* is created. To obtain the complete vascular system, more than one seed point might be required. If the vessel tracking produces an undesired result, e.g. by propagating into bones, it can be reverted (undo operation) and rerun after inserting separation objects to prevent tracking towards specific directions. So far, the described algorithm works properly if vessels are not touching any bone and the vessel tree does not have any discontinuities. Cases of vessels touching bone and small discontinuities are handled during vessel tracking, as further explained below. Large vascular discontinuities caused by long-segment occlusions or artifactual obscuration by metal implants (e.g. hip joint implants) are treated later in the graph generation stage.

3.2.1. Vessels touching bone

A large difference in size between the current vessel island and its candidate island could be caused by a vessel touching bone. To avoid tracking the bone instead of the blood vessel, we utilize the characteristics of vessel islands, depending on the transverse slice location within the data set, i.e. proximal or distal. As previously mentioned, proximal vessel voxels touching bones are usually labeled as strong voxels. Contrary, distal blood vessels are very small and, apart from calcifications, are characterized by much lower intensity values than bone. In such situations, vessel voxels are labeled as weak foreground. Fig. 3 illustrates these two cases of vessel propagation, from the current slice to one of its adjacent slices.

The first case addresses the proximal part, i.e. **upper half**, of the data set (the upper part of Fig. 3). The current slice contains a vessel island and a foreground island. The adjacent slice contains a single island, varying substantially from the size of the current vessel island, and being composed of strong and weak voxels. Our proposed method eliminates all the weak voxels from the adjacent slice, located in the neighborhood N of the current vessel island's border (the area between the island and the background). This splits the candidate island into two disconnected parts, one that is marked as vessel and another one that remains labeled as strong. If there are still strong voxels connecting two distinct anatomical foreground elements (in our case bone and vessel), the algorithm cannot divide the candidate island and the tracking stops.

In the distal part, i.e. **lower half**, of the data set, vessel tissue that touches bone contains mostly weak voxels. The lower part of Fig. 3 illustrates this case, where the current slice contains a foreground island and the current vessel island. The adjacent slice contains a single island, again composed of strong and weak voxels, but in this case the vessel

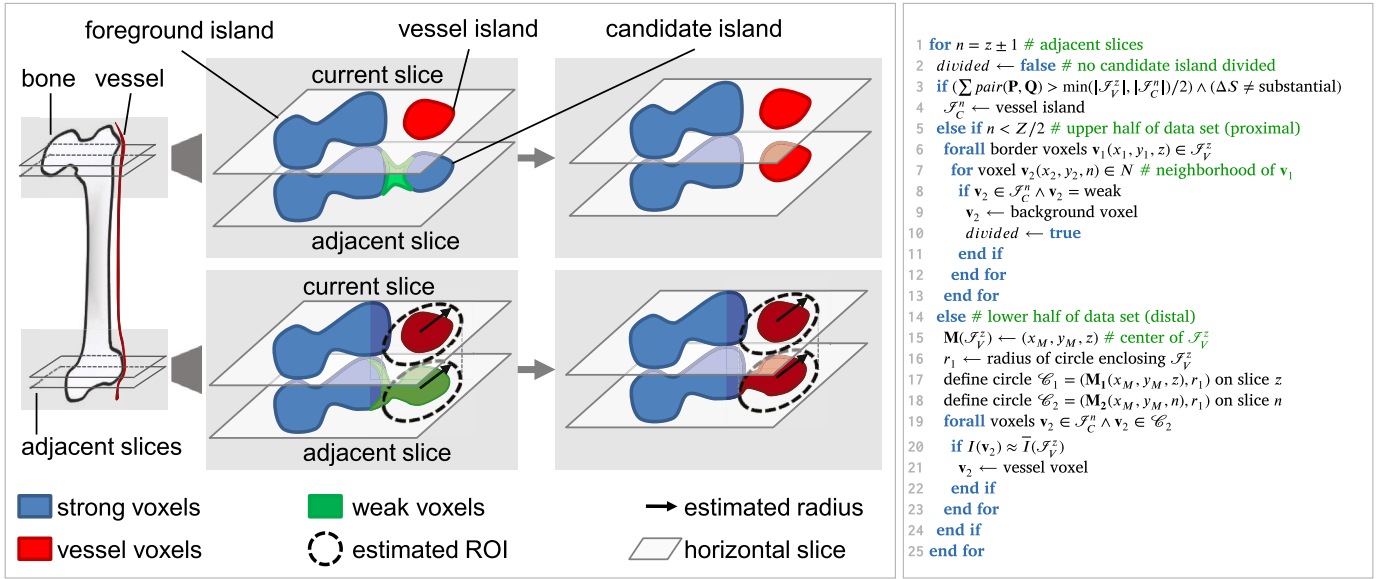


Fig. 3. The left illustration shows how the problem ‘vessel touching bone’ is solved depending on the z-position (proximal vs. distal) in the data set. The corresponding pseudocode is shown on the right side.

consists only of weak voxels. Since the proximal strategy would remove the entire vessel tissue on the adjacent slice, we have to choose another approach. We compute the center $\mathbf{M}(\mathcal{F}_V^z)$ of the current vessel island as the average position of all its contained voxels and radius r_1 of its circumscribed circle. This circle is then propagated to the adjacent slice to split the candidate island.

A foreground voxel inside this circle is marked as belonging to a vessel island if its intensity value $I(\mathbf{v})$ does not differ significantly from those of the current vessel island, i.e., if $(I_{\min}(\mathcal{F}_V^z) - I(\mathbf{v}) \leq 50)$ and $(I(\mathbf{v}) - I_{\max}(\mathcal{F}_V^z) \leq 50)$; otherwise the voxel remains unchanged. $I_{\min}(\mathcal{F}_V^z)$ and $I_{\max}(\mathcal{F}_V^z)$ represent the minimum and the maximum intensity values within the current vessel island, respectively.

To successfully separate vessels from bone, we have to find the balance between preserving vessels and stopping the propagation of vessel tissue to bone. Factors such as the anatomy of the patient, the contrast agent, or the imaging modality influence this balance. If vessels cannot automatically be separated from bone, user-specified separation objects (planes and cylinders) can prevent vessels spreading into bone.

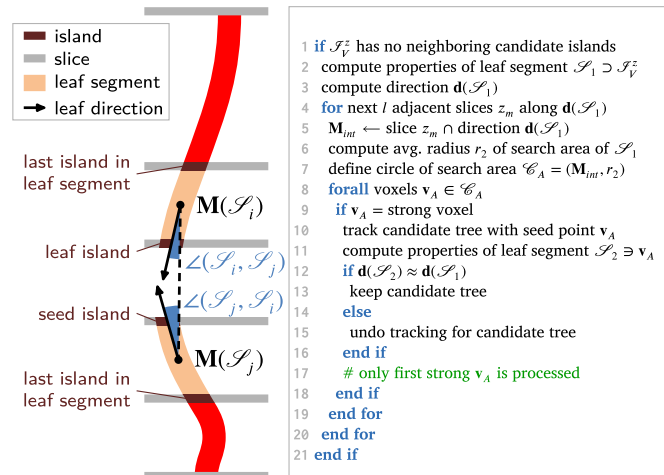


Fig. 4. The left illustration shows the linking of ‘small vessel discontinuities’ in vessel paths. The corresponding pseudocode is shown on the right side.

3.2.2. Small vessel discontinuities

The second challenge consists of small discontinuities of the vessel paths (centerlines), which occur especially in the area below the knee. The vessel propagation stops when we encounter a vessel island that has no neighboring islands other than the island that led to its discovery. We deal with this problem (see Fig. 4) in the vessel tracking stage. Our algorithm searches for a new candidate vessel segment in a local neighborhood around the point where the propagation was stopped. When a candidate is found, we use a cost function to determine whether it can be connected to a tracked vessel segment. This function represents the probability that two segments belong to the same vessel. If the cost function of the candidate and tracked vessel segment is below a global threshold, they are connected. To calculate this cost function, we propagate the vessel tissue and store per slice the average position, size, minimum, average, and maximum intensity for each detected vessel island, as well as its connectivity with vessel islands of adjacent slices. Before introducing the cost function, however, we describe leaf islands and segments and how the direction of a leaf segment is determined.

A vessel island with a single neighboring island in the tracked partial vessel tree is called a *leaf island* if it does not contain a seed point (it is not a seed island). By connecting the last k vessel islands in reverse order of the propagation, starting with the detected leaf island, a *leaf segment* is created. Also, by connecting the first k vessel islands, in the order of the propagation, starting with the seed island, another leaf segment is created. An example of two leaf segments (the first obtained from a leaf island and the second from a seed island) is given in Fig. 4.

For all leaf segments \mathcal{S}_i of a partial vessel tree, we compute the following properties: the center of the leaf segment, the minimum, average and maximum intensity, the minimum, average and maximum size of the vessel islands within the leaf segment. The direction \mathbf{d} of a leaf segment \mathcal{S} is defined as

$$\mathbf{d}(\mathcal{S}) = (\mathbf{M}(\mathcal{S}_1) - \mathbf{M}(\mathcal{S})) + (\mathbf{M}(\mathcal{S}_1) - \mathbf{M}(\mathcal{S}_k)), \quad (6)$$

where $\mathbf{M}(\mathcal{S})$ is the leaf segment’s center (average position of all contained voxels), $\mathbf{M}(\mathcal{S}_1)$ is the center of the leaf segment’s first vessel island \mathcal{S}_1 , and $\mathbf{M}(\mathcal{S}_k)$ is the center of the last (k^{th}) leaf segment’s vessel island \mathcal{S}_k .

Our algorithm searches for voxels from the *vessel + bone* class, in the next l slices adjacent to the current leaf island, in the direction of the stopped propagation. The search area is determined as follows: on the

investigated slice (one of the l adjacent slices), we determine the intersection point \mathbf{M}_{int} with the ray going from position $\mathbf{M}(\mathcal{S})$ in direction $\mathbf{d}(\mathcal{S})$ of the current leaf segment \mathcal{S} . We then compute a circle with center in \mathbf{M}_{int} and radius $r_2 = \sqrt{|\mathcal{S}_{vi}|/\pi}$, where $|\mathcal{S}_{vi}|$ is the average size of the current leaf segment's vessel islands. In case a strong foreground voxel is encountered inside this circle, the island containing that voxel is extracted. If the size and intensity of this island do not substantially deviate from the average size and intensity of the islands contained in the leaf segment, the discovered voxel is marked as a seed point and inserted into a queue of seed points q_{sp} . After the current vessel tracking stage completely stops, i.e., queue q_{sp} does not contain any vessel islands anymore, another tracking stage starts with the first element dequeued from q_{sp} .

Another tracking stage starts with a seed point from q_{sp} and extracts only a candidate partial tree. A leaf segment is created for this tree by connecting the first k vessel islands from the tree in order of propagation, starting with its seed island. After this, it is decided whether the parent leaf segment and the candidate one should be connected or not.

Two orientation measures, $\angle_{ij} = \angle(\mathcal{S}_i, \mathcal{S}_j)$ and $\angle_{ji} = \angle(\mathcal{S}_j, \mathcal{S}_i)$, are computed for the two leaf segments $(\mathcal{S}_i, \mathcal{S}_j)$, based on their center positions and directions:

$$\angle(\mathcal{S}_i, \mathcal{S}_j) = \frac{\mathbf{d}(\mathcal{S}_i) \cdot (\mathbf{M}(\mathcal{S}_i) - \mathbf{M}(\mathcal{S}_j))}{\|\mathbf{d}(\mathcal{S}_i)\| \cdot \|\mathbf{M}(\mathcal{S}_i) - \mathbf{M}(\mathcal{S}_j)\|}. \quad (7)$$

As illustrated in Fig. 4, \angle_{ij} represents the cosine of the angle between the direction $\mathbf{d}(\mathcal{S}_i)$ of the parent leaf segment and the vector from the center $\mathbf{M}(\mathcal{S}_i)$ of the parent leaf segment to the center $\mathbf{M}(\mathcal{S}_j)$ of the candidate one. Similarly, \angle_{ji} depicts the cosine of the angle between the direction $\mathbf{d}(\mathcal{S}_j)$ of the candidate leaf segment and the vector from the center of the candidate leaf segment to the center of the parent.

We introduce a cost function C_D for connecting small vessel discontinuities. This cost is defined for the parent leaf segment and the candidate one, as the weighted sum of four characteristics, namely the difference in distance, orientation, intensity, and size:

$$C_D = \sum_{n=1}^4 w_n C_n, \quad (8)$$

with w_n being the weight of the respective characteristic C_n .

Leaf segments located closer to each other have a high probability of being connected. C_1 is the normalized distance between the center positions of the parent leaf segment (\mathcal{S}_i) and the candidate one (\mathcal{S}_j) , defined as

$$C_1 = \frac{\|\mathbf{M}(\mathcal{S}_i) - \mathbf{M}(\mathcal{S}_j)\|}{\|\mathbf{V}_{diag}\|}, \quad (9)$$

with vector $\mathbf{V}_{diag} = (X, Y, Z)$ and X, Y and Z being the extent of the data set.

The difference in orientation, C_2 is defined as follows:

$$C_2 = \frac{(1 - \angle(\mathcal{S}_i, \mathcal{S}_j)) + (1 - \angle(\mathcal{S}_j, \mathcal{S}_i))}{2}, \quad (10)$$

where $\angle(\cdot, \cdot)$ is defined in Equation (7). A small C_2 value indicates a direction continuity in the vessel path.

A vessel path should also be characterized by a continuity in intensity distributions. Therefore, C_3 depicts the normalized difference in intensity between the parent and the candidate leaf segment:

$$C_3 = \frac{|I_{max}(\mathcal{S}_i) - I_{max}(\mathcal{S}_j)| + |I_{min}(\mathcal{S}_i) - I_{min}(\mathcal{S}_j)|}{2 \cdot I_{max}(\mathcal{S})}, \quad (11)$$

with $I_{min}(\mathcal{S})$ and $I_{max}(\mathcal{S})$ being the minimum and maximum intensity value of the leaf segments. The maximum intensity of the entire data set is given by $I_{max}(\mathcal{S})$.

C_4 , refers to the normalized size difference between two leaf segments, and is defined as

$$C_4 = \frac{|A(\mathcal{S}_i) - A(\mathcal{S}_j)| + |a(\mathcal{S}_i) - a(\mathcal{S}_j)|}{2 \cdot X \cdot Y}, \quad (12)$$

$$a(\mathcal{S}) = \{|\mathcal{S}| : \mathcal{S} \in \mathcal{S}, |\mathcal{S}| \leq |\tilde{\mathcal{S}}|, \forall \tilde{\mathcal{S}} \in \mathcal{S}\}, \quad (13)$$

$$A(\mathcal{S}) = \{|\mathcal{S}| : \mathcal{S} \in \mathcal{S}, |\mathcal{S}| \geq |\tilde{\mathcal{S}}|, \forall \tilde{\mathcal{S}} \in \mathcal{S}\}, \quad (14)$$

with $a(\mathcal{S})$ and $A(\mathcal{S})$ representing the size of the smallest and largest vessel island of segment \mathcal{S} , respectively. A small value of C_4 indicates continuity in vessel size.

We used the following configuration of weights for the cost function C_D in the vessel tracking stage: $w_1 = 1, w_2 = 2, w_3 = 1, w_4 = 1$. Since the orientation between the parent and candidate segments is an important factor, we gave it a higher weight.

If the orientation measures \angle_{ij} and \angle_{ji} depict a small difference in direction between the parent leaf segment and the candidate one, i.e. $(\angle_{ij} > 0.8) \wedge (\angle_{ji} > 0.8)$, and the previously computed cost has a value below a chosen threshold, i.e., 0.6, the two leaf segments are connected, and the candidate tree is considered a real vessel tree. Otherwise, the tracking process for the candidate tree is reverted and all the seed points from q_{sp} that were discovered during its tracking stage are removed without being processed.

This entire process continues until q_{sp} is empty. The tracking stage is recursive, but all the constraints for propagating the vessel tree ensure that the process terminates eventually. Thus, the vessel label will not propagate to bone or other tissue. In our experiments, the values of k and l were established empirically and set to $k = l = 10$.

3.3. Graph generation

The result of the previous stage is the entire vasculature that is composed of one or more partial vessel trees, each containing a number of connected vessel islands. However, this representation is not suitable

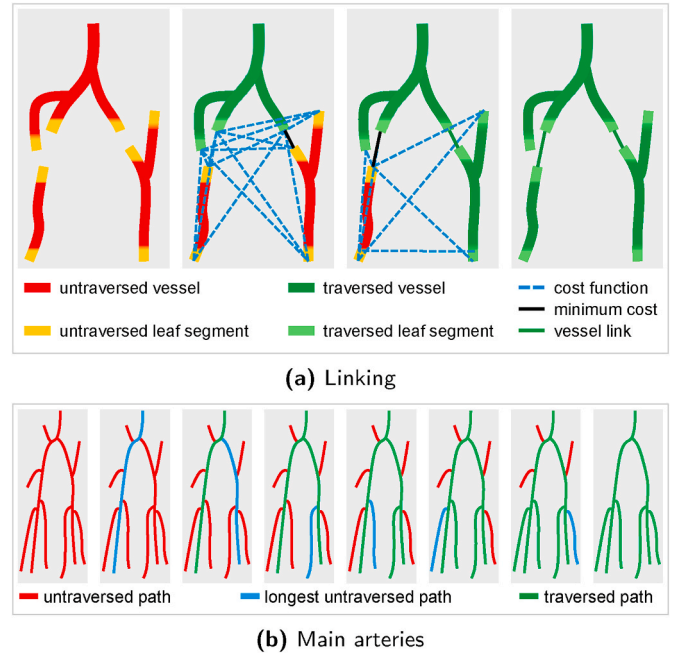


Fig. 5. Graph generation. (a) illustrates the linking of partial vessel trees (Step 12). Disconnected vessel segments are joined, based on the minimum cost to all other vessel segments. (b) demonstrates how the main arteries are determined (Step 14) for PAD investigations.

for an analysis or a visualization such as CPR. Therefore, we organize the vessel tree in a graph-like data structure (see Fig. 1, Steps 12 to 16) consisting of 3D points belonging to the centerlines of the main arteries. Multiple partial vessel trees are linked together (Step 12) to form a single vessel tree of the entire relevant vascular system, as outlined in Fig. 5a.

Linking partial vessel trees is similar to reconnecting small vessel discontinuities (recall Section 3.2.2), but with the following difference: while the vessel tracking stage performs a local search to find potential candidate vessel segments that could be connected to already tracked segments, the current stage does not perform a search but connects all partial vessel trees. By initially starting from a partial vessel tree and iteratively identifying and adding the most likely connection to another partial vessel tree, we build the final and complete vessel tree. The most proximal seed island is selected as the seed island and its partial vessel tree is traversed using a breadth-first search (BFS) heuristic. The cost function C_G for linking the partial vessel trees to the complete vessel tree is defined for all pairs $(\mathcal{S}_i, \mathcal{S}_j)$ of leaf segments, with i being the traversed leaf segment during the BFS, j the untraversed segment, and $i \neq j$. The cost function consists of the weighted sum of seven leaf segment characteristics:

$$C_G = \sum_{n=1}^7 w_n C_n, \quad (15)$$

with w_n being the weight of the respective characteristic C_n , and the cost being inversely proportional to the connection probability, i.e., the smallest value indicates the highest probability. The first four characteristics are the same as for the cost function for small vessel discontinuities, recall Equation 8.

The fifth characteristic C_5 ensures that proximal leaf segments of an untraversed vessel tree have a higher probability of being connected to a traversed leaf segment than distal leaves:

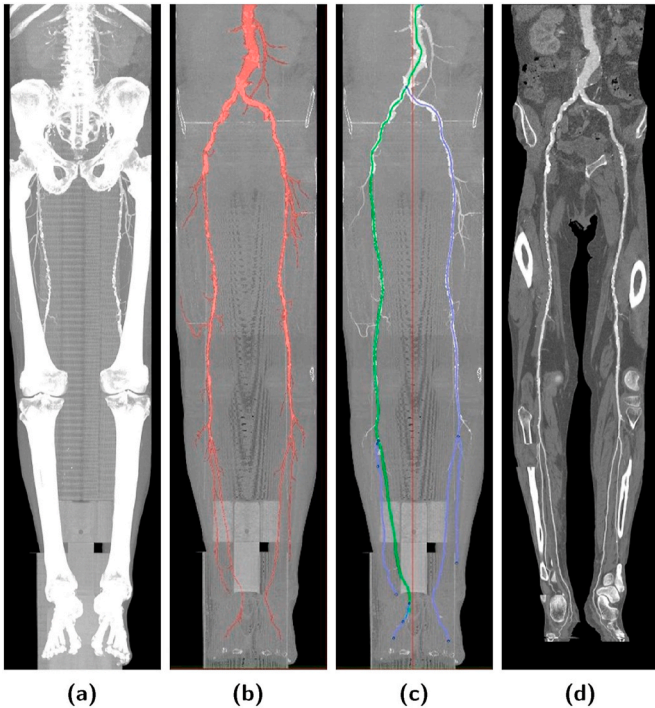


Fig. 6. A standard peripheral CTA case. (a) presents a MIP of the entire raw data set. (b) shows a MIP without bones, after vessels and bones were segmented with our approach. (c) shows the tracked vessel tree (blue) with a selected path (green). (d) displays a mpCPR of the entire vessel tree. (For interpretation of the references to colour in this figure legend, the reader is referred to the web version of this article.)

$$C_5 = \frac{z(\mathcal{S}) - z_{\min}(v)}{z_{\max}(v) - z_{\min}(v)}, \quad (16)$$

with $z(\mathcal{S})$ being the z -coordinate of the leaf island $\mathcal{S} \in \mathcal{S}_j$, $z_{\min}(v)$ being the minimum and $z_{\max}(v)$ being the maximum z -coordinate of the partial vessel tree v with $\mathcal{S}_j \in v$.

The intensity of the voxels located along the path connecting the two leaf segments \mathcal{S}_i and \mathcal{S}_j is also an indicator of vessel continuity. It is computed as follows:

$$C_6 = \frac{\sum_{z=\min(z(\mathcal{S}_k), z(\mathcal{S}_i))-1}^{\max(z(\mathcal{S}_k), z(\mathcal{S}_i))+1} [H(\mathcal{S}_i) + H(\mathcal{S}_j) - 2\bar{I}(\mathcal{S}_z^z)]}{2 \cdot (|z(\mathcal{S}_i) - z(\mathcal{S}_k)| - 1) \cdot I_{\max}(\mathcal{S})}, \quad (17)$$

$$H(\mathcal{S}) = \frac{I_{\min}(\mathcal{S}) + I_{\max}(\mathcal{S})}{2}, \quad (18)$$

where $\mathcal{S}_k \in \mathcal{S}_i$, $\mathcal{S}_l \in \mathcal{S}_j$, $\bar{I}(\mathcal{S})$ is the average intensity value of a vessel island, and $H(\mathcal{S})$ is the average of the minimum and maximum intensity values of a vessel segment. The path that connects the two leaf segments is determined by creating an artificial (i.e., it was neither discovered during segmentation nor tracking) circular vessel island \mathcal{S}_z^z on each slice between $z(\mathcal{S}_k)$ and $z(\mathcal{S}_l)$. The position of this new island is the intersection point of the current slice with the line passing through the two points $\mathbf{M}(\mathcal{S}_k)$ and $\mathbf{M}(\mathcal{S}_l)$. The size of the island is linearly interpolated between the average sizes of the corresponding two leaf segments. If the average intensity of these artificial islands along the path does not differ significantly from the minimum and maximum intensities of the two leaf segments, C_6 will be small.

C_7 , the last characteristic of the proposed cost function, ensures that larger leaf segments have priority during linking, as compared to smaller ones. Since the main arteries are usually thicker than secondary arteries or veins, they should be connected first. It is computed as

$$C_7 = 1 - \frac{a(\mathcal{S}_i) + A(\mathcal{S}_i) + a(\mathcal{S}_j) + A(\mathcal{S}_j)}{4 \cdot X \cdot Y}. \quad (19)$$

In our implementation, the following configuration of weights for the cost function C_G was used: $w_1 = 3$, $w_2 = 8$, $w_3 = 1$, $w_4 = 1$, $w_5 = 2$, $w_6 = 1$ and $w_7 = 1$.

After identifying the two leaf segments with the minimum cost

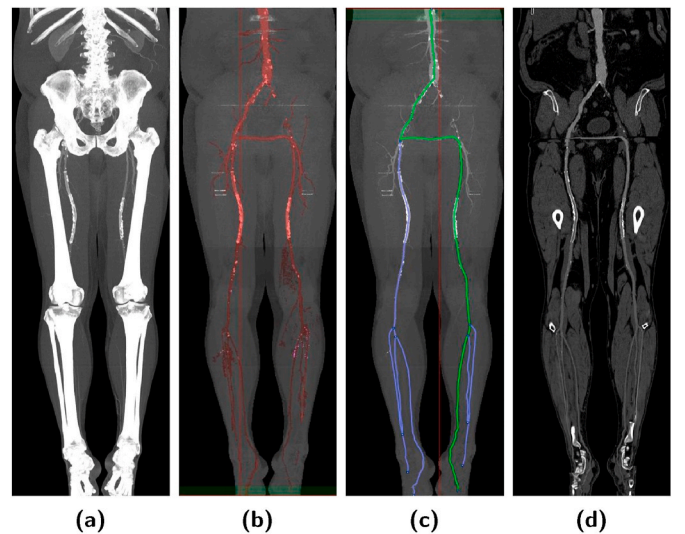


Fig. 7. Example of a CTA data set with a cross-over bypass and two stents. (a) presents a MIP of the entire raw data set. (b) shows a MIP without bones, after vessels and bones were segmented with our approach. (c) shows that the vessel tree was properly tracked through the bypass and the relevant paths were determined correctly. (d) displays a mpCPR of the entire vessel tree.

function, we linearly interpolate a path between them. The leaf island of the untraversed leaf segment represents the new seed island for the BFS. This process is repeated until no more untraversed partial vessel trees exist. The result of this step is a single vessel tree that contains all the previously tracked partial trees. This solves the problem of large discontinuities in vessel paths.

After determining a connected set of voxels belonging to blood vessels, we compute the centerlines using skeletonization (Step 13) [21]. Subsequently, we determine the relevant blood vessels (Step 14). As it is sufficient for PAD to evaluate the vessel tree from the aortic root to six distal arteries (three on each side, recall Section 3, second paragraph), we model the vascular system as a hierarchical tree structure from the abdominal aorta to the feet. The root node is defined as the most proximal voxel, i.e., with the minimal z -coordinate. Inspired by the human anatomy, our method assumes each leaf node (distal voxel) of a main artery is located in the lower third part of the data set. A path between the root node and each leaf node is computed with a BFS traversal, computing the distance between the two nodes. The leaf node with the longest distance to the root node is identified as the last node of one of the main arteries. The points on the first determined main artery are marked once visited. The next main arteries are identified (and then visited) by extracting the leaf nodes with the largest number of unvisited voxels located on the path to the root node. Fig. 5b illustrates our approach of constructing the paths of the main arteries. If a patient has an amputated limb, not all paths can be determined, and a manual adjustment is necessary.

Once the main arteries are determined, the radii along their centerlines are computed (Step 15). The data set is re-sampled at each node in the tree in order to obtain a cross-section, or slice, perpendicular to the direction of the centerline. The voxels on this oblique slice either belong to the *vessel* or *other tissue* class. The estimated radius is the maximal Euclidean distance from the centerline point to the voxels of the *vessel* class. The centerlines of the main arteries, along with their associated radii, are converted into a graph representation (Step 16) and smoothed using B-spline re-sampling.

4. Results and discussion

Our proposed algorithm processes a common peripheral CTA case (see Fig. 6 and Entry 7 in Table 1) without any problems. As clearly shown in Fig. 6b, the main arteries are properly detected and converted to a graph representation (see Fig. 6c). A set of mpCPR images (see Fig. 6d) of the extracted vascular system is then generated from multiple viewing angles for inspection by a radiologist, as usual in clinical routine. The ability to display each of the curved reformatted vessels simultaneously is critical for efficient review and diagnosis, since the tree-like spatial arrangement provides the visual clue for identification of anatomic segments. The familiar spatial arrangement is also maintained at different viewing angles, which are required to visually gauge the severity of eccentric lesions. The mpCPR visualization technique facilitates a thorough, yet time-efficient review of the peripheral arterial tree [42]. In particular, the diagnostic accuracy of less experienced radiologists seems to improve with mpCPRs compared to regular multi-planar reformations (MPRs).

Another clinical case is presented in Fig. 7 (Entry 8 in Table 1). This case comprises two algorithmic challenges, a cross-over bypass (vessel of different spatial orientation) and two stents. Both are properly handled by our approach, and the resulting mpCPR is presented in Fig. 7d.

Vessels Touching Bone Fig. 8a presents several slices of a data set containing vessels that are very close to bone tissue. Even if in some slices (see slice 987) vessels are connected to bone in the segmentation stage, only the vessel tissue is determined in the subsequent (tracking) stage and the vessel is correctly tracked in these slices. To our knowledge, this is the first algorithm to solve this problem with minimal user interaction. Available solutions either require a high amount of user

interaction or simply fail to separate bones from adjacent vessels.

Small Vessel Discontinuities A data set with many small vessel discontinuities is shown in Fig. 8b. In this example, our proposed method reconnected all but one discontinuity in the tracking stage. Only a single additional seed point solved this problem and the remaining discontinuity was handled during linking (Step 12).

Bone-like Regions Stents and calcifications do not have the same characteristics as vessel tissue. They have much higher intensity values,

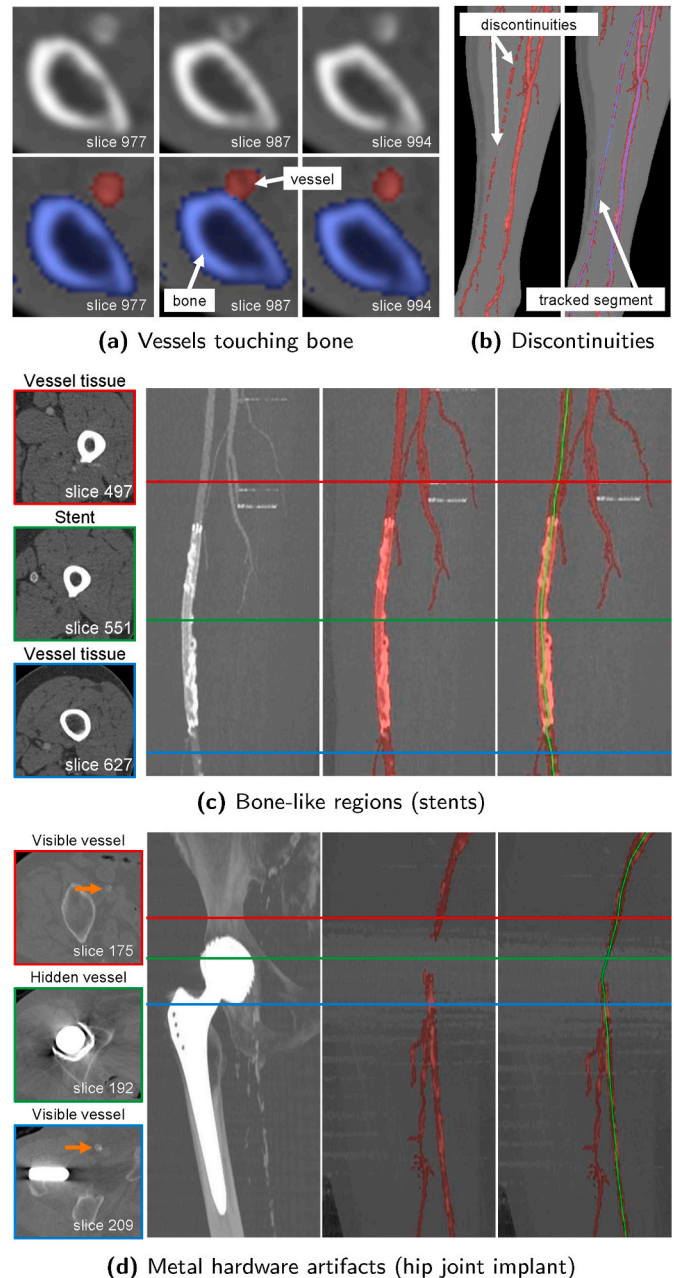


Fig. 8. Solved challenging cases. (a) shows that our approach correctly tracks a small vessel even when it touches a bone. (b) presents a correctly tracked vessel tree despite many small discontinuities. (c) demonstrates the correct tracking of a stent, even if the intensity values of the vessel and stent are quite different. The corresponding axial slices are shown on the left, followed by a coronal MIP, the segmented vessels, and on the right the vessel centerline, respectively. (d) clearly conveys the strengths of our linking approach in dealing with larger discontinuities caused by metal implants. The corresponding axial slices are shown on the left, followed by a coronal MIP, the segmented vessels with a large discontinuity caused by the metal implant, and on the right the correctly connected vessel centerline.

comparable to those of bone tissue. Fig. 8c shows a data set with a stent that is correctly tracked as part of the vessel tree using our proposed technique. Since the size of stents and calcified tissue within a single slice is comparable (or smaller) to that of vessel tissue, stents can be properly tracked.

Metal Hardware Artifacts Prosthetic hip or knee joint implants or other orthopedic hardware such as fixation screws and plates result in considerable metal artifacts in CTA data sets (see Fig. 8d). On the left, artifacts (dark bands and streak noise) caused by an artificial hip joint are presented in three axial slices. In slices 175 and 209, the vessel tissue is visible, but in slice 192 it is completely obscured by the artifacts. In the event that manual user interaction is necessary, our approach minimizes effort. In this difficult case, only one additional user-specified seed point was required. During linking (Step 12), the separate vessel segments were correctly connected and, subsequently, the vessel tree was successfully constructed.

5. Evaluation

To evaluate our approach, we compared our results with those of the semi-automatic approach currently used in cooperating hospitals [17]. The latter approach starts with the automatic identification of bone and vessel tissue using thresholds, region-growing, and morphological operations. The user can then manually adjust the proposed labels slab-wise (a slab comprises a series of consecutive slices, usually around 30), either by assigning them directly or by using a combination of 3D region-growing and separation objects that prevent regions from growing outside the desired boundaries. Once vessels and bones are adequately labeled, the corresponding vessels are traced as the shortest path between user-defined source and target points, based on density and gradient information. Vascular discontinuities are treated manually by interpolating centerlines with many contiguous linear segments, a cumbersome and time-consuming procedure.

We conducted two studies, a pilot study (see Table 1) carried out by a computer scientist and a clinical study (see Table 2) performed by a radiology technologist. The workflow was designed to resemble the clinical environment in a tertiary care facility where subspecialty care is routinely provided for patients with PAD. In both studies, we measured the

- segmentation time (**Tseg**, Step 1 to Step 6),
- number of seed points (**SP**, Step 7),
- number of undo operations (**U**),
- tracking time (**Ttrack**, Step 7 to Step 11),
- automatic vessel tree generation time (**Tgen**), and
- total time (**Ttotal**).

Table 1

The pilot study was carried out by a computer scientist and compared the accuracy of our approach with the method used by our clinical partners. We assessed the segmentation time (**Tseg**), number of seed points (**SP**), number of undo operations (**U**), tracking time (**Ttrack**), automatic vessel tree generation time (**Tgen**), total time (**Ttotal**), true positive rate (**TPR**), true negative rate (**TNR**), positive predictive value (**PPV**), negative predictive value (**NPV**), accuracy (**ACC**), and **Dice** coefficient. Timings are given in [mm:ss].

No	Performance						Accuracy						
	Tseg	SP	U	Ttrack	Tgen	Ttotal	Size	TPR	TNR	PPV	NPV	ACC	Dice
1	0:31	6	1	2:57	0:44	4:18	$512^2 \times 1151$	0.9165	0.9997	0.8287	0.9999	0.9996	0.8704
2	0:20	6	0	0:43	0:15	1:24	$512^2 \times 0766$	0.9188	0.9998	0.8240	0.9999	0.9998	0.8688
3	0:35	9	0	1:30	0:32	2:46	$512^2 \times 1236$	0.9100	0.9999	0.9527	0.9999	0.9998	0.9309
4	0:31	4	0	1:43	0:30	2:48	$512^2 \times 1147$	0.9057	0.9998	0.8146	0.9999	0.9997	0.8577
5	0:33	3	1	3:44	0:42	5:02	$512^2 \times 1206$	0.9428	0.9998	0.7709	1.0000	0.9997	0.8482
6	0:36	9	0	3:16	0:41	4:42	$512^2 \times 1170$	0.9205	0.9999	0.9067	0.9999	0.9998	0.9136
7	0:52	1	0	0:50	0:57	2:40	$512^2 \times 1799$	0.9328	1.0000	0.9823	0.9999	0.9999	0.9569
8	0:37	5	2	6:02	0:48	7:33	$512^2 \times 1304$	0.9575	0.9999	0.9304	0.9999	0.9998	0.9438
9	0:38	4	3	8:00	0:23	9:05	$512^2 \times 1250$	0.9551	0.9999	0.9347	0.9999	0.9998	0.9448
μ	0:35	5	1	3:11	0:36	4:28	$512^2 \times 1225$	0.9289	0.9999	0.8828	0.9999	0.9998	0.9039
σ	0:08	3	1	2:27	0:14	2:29	$512^2 \times 0265$	0.0192	0.0001	0.0741	0.0000	0.0001	0.0426

The segmentation stage of our approach was implemented on the GPU using CUDA, while all the other steps were implemented on the CPU. All timings are given in minutes and seconds (mm:ss).

The aim of the **pilot study** ($N = 9$) was a feasibility assessment of our proposed approach. It was carried out by a computer scientist, a coauthor and developer of our algorithm. Since the algorithmic details were known, it was clear where to place seed points and how to correct problems efficiently. With this in mind, we explicitly designed the pilot study in such a way that we only assessed whether the algorithm was sufficiently accurate for a larger clinical study. In addition to the usual parameters, the following ones were measured as well:

- true positive rate (**TPR**) or sensitivity, the percentage of vessel tissue identified correctly as vessel,
- true negative rate (**TNR**) or specificity, the percentage of voxels belonging to other tissue that were correctly labeled as such,
- positive predictive value (**PPV**) or precision,
- negative predictive value (**NPV**),
- accuracy (**ACC**), the number of correctly labeled voxels (either belonging to vessels or other tissue) compared to the total number of voxels in a data set, and
- **Dice** coefficient.

All measurements were taken on an Intel i7-2600 K 3.40 GHz processor with 8 GB RAM and an Nvidia GeForce GTX 590 GPU with 1.5 GB RAM. Overall, it took $4:28 \pm 2:29$ [mm:ss] to segment and track the required arteries with only 5 ± 3 seed points on average. The tracking was rarely reverted (undo, on average only once) to correct seed points or specify separation planes. We achieved a TPR of $92.89\% \pm 1.92\%$, a PPV of $88.28\% \pm 7.41\%$, and a Dice coefficient of $90.39\% \pm 4.26\%$. The reason for the lower PPV is that our method occasionally segmented a few secondary vessels as well (false positives), whereas medical experts usually focus on finding only the relevant arteries in the vessel tree (recall Section 3, second paragraph). However, as these secondary vessels do not affect determining the main arteries, the lower PPV is not considered an issue in the routine. We obtained a TNR of $99.99\% \pm 0.01\%$, a NPV of 99.99% , and an accuracy of $99.98\% \pm 0.01\%$. The reason for the very high TNR and NPV is that our approach very accurately identifies true negatives, i.e. other tissue or background. As expected, there was a considerable difference in terms of completion time between our approach and the timings reported by Kanitsar et al. [17] (30–45 min). Therefore, we conducted the larger, second study.

The **clinical study** ($N = 24$) was carried out by a radiology technologist (a coauthor) in one of our collaborating hospitals (see Table 2). To obtain a satisfactory vessel tree, it is usually adjusted manually by adding or removing control points. These points are located either at

Table 2

The clinical study was carried out by a radiology technologist and measured the time and number of interactions until a satisfactory result was reached. We compared our approach (blue) with the routine approach (gray). We assessed the segmentation time (**Tseg**), number of seed points (**SP**), number of undo operations (**U**), tracking time (**Ttrack**), automatic vessel tree generation time (**Tgen**), total time (**Ttotal**), number of manually placed control points (**CP**), number of deleted control points (**dCP**), time to obtain a satisfiable vessel tree (**Tvtree**), automatic segmentation time (**Taseg**), and manual segmentation time (**Tmseg**).

No	Proposed Approach									Routine Approach						Tdiff	Perf
	Tseg	SP	U	Ttrack	Tgen	CP	dCP	Tvtree	Ttotal	Taseg	Tmseg	CP	dCP	Tvtree	Ttotal		
1	0:21	46	0	10:39	0:19	102	0	23:40	34:59	0:03	19:40	56	7	15:10	34:53	-0:06	1.00
2	0:16	13	1	8:52	0:04	54	0	13:58	23:10	0:05	15:09	47	5	11:53	27:07	3:57	1.17
3	0:22	15	1	6:33	0:25	30	0	9:39	16:59	0:03	22:20	73	10	16:55	39:18	22:19	2.31
4	0:16	9	0	5:19	0:13	41	5	16:54	22:42	0:05	5:06	53	8	11:22	16:33	-6:09	0.73
5	0:19	23	5	10:29	0:14	63	9	10:33	21:35	0:04	16:20	39	1	11:01	27:25	5:50	1.27
6	0:16	19	4	10:44	0:20	29	1	6:00	17:20	0:04	16:24	56	4	12:06	28:34	11:14	1.65
7	0:16	11	0	3:19	0:12	56	3	13:41	17:28	0:05	10:13	35	2	7:52	18:10	0:42	1.04
8	0:16	9	2	3:01	0:17	38	4	9:01	12:35	0:04	8:25	55	3	9:52	18:21	5:46	1.46
9	0:15	7	1	4:16	0:08	44	6	12:00	16:39	0:04	8:30	39	3	11:14	19:48	3:09	1.19
10	0:16	9	4	9:41	0:13	26	4	12:33	22:43	0:04	20:03	99	10	17:37	37:44	15:01	1.66
11	0:15	11	1	2:54	1:34	55	5	11:18	16:01	0:04	14:07	48	3	10:33	24:44	8:43	1.54
12	0:19	12	2	5:53	0:24	44	3	10:30	17:06	0:05	14:40	54	3	10:20	25:05	7:59	1.47
13	0:17	7	2	14:32	0:09	61	2	11:23	26:21	0:04	10:23	69	2	9:16	19:43	-6:38	0.75
14	0:20	4	1	1:52	0:15	38	5	8:02	10:29	0:05	13:07	80	3	16:00	29:12	18:43	2.79
15	0:15	2	0	0:52	0:19	29	1	3:41	5:07	0:05	13:45	73	7	19:01	32:51	27:44	6.42
16	0:18	5	0	3:50	0:14	40	1	6:35	10:57	0:04	18:54	66	2	19:03	38:01	27:04	3.47
17	0:18	6	0	2:26	0:20	25	0	4:49	7:35	0:04	13:06	63	10	18:47	31:57	24:22	4.21
18	0:19	15	2	6:23	0:19	45	4	6:07	13:08	0:04	24:00	60	6	13:46	37:50	24:42	2.88
19	0:18	4	0	3:11	0:11	47	3	8:16	11:38	0:06	14:21	51	5	10:39	25:06	13:28	2.16
20	0:15	8	0	10:15	0:12	64	2	11:34	22:16	0:04	26:30	116	8	20:02	46:36	24:20	2.09
21	0:19	7	1	4:29	0:20	51	7	12:33	17:41	0:05	13:25	32	1	8:32	22:02	4:21	1.25
22	0:17	5	0	3:06	0:23	44	0	11:10	14:56	0:04	21:23	39	1	9:20	30:47	15:51	2.06
23	0:17	6	1	4:02	0:06	38	2	7:48	12:13	0:03	11:34	64	4	13:56	25:33	13:20	2.09
24	0:16	6	2	12:18	0:08	53	3	13:28	26:10	0:05	16:18	56	9	14:36	30:59	4:49	1.18
μ	0:17	11	1	6:12	0:18	47	3	10:38	17:24	0:04	15:19	59	5	13:17	28:40	11:16	1.99
σ	0:02	9	1	3:46	0:17	16	2	4:14	6:44	0:00	5:12	20	3	3:44	7:45	10:14	1.27

Description	Proposed	Routine	Shapiro-Wilk ($p < 0.05$)	Paired t-test ($p < 0.05$)
Segmentation times	Tseg + Ttrack	Taseg + Tmseg	0.7058	4.17e-08*
Vessel tree construction times	Tgen + Tvtree	Tvtree	0.5534	0.08571
Control point additions	CP	CP	0.9956	0.03417*
Control point deletions	dCP	dCP	0.8006	0.04625*
Total time	Ttotal	Ttotal	0.3129	0.00001792*

*significant difference ($p < 0.05$)

branches or end points of a vessel. In difficult cases, e.g. a vessel occlusion, the vessel centerline is manually defined by inserting consecutive control points. Since the correct placement of such control points is time-consuming, we made the following additional measurements:

- number of manually placed control points (**CP**),
- number of deleted control points (**dCP**),
- time to obtain a satisfiable vessel tree (**Tvtree**),
- automatic segmentation time (**Taseg**), and
- manual segmentation time (**Tmseg**).

All measurements were taken on an Intel i5-7500 3.40 GHz processor with 32 GB RAM and an Nvidia GTX 1070 GPU with 8 GB RAM. We compared our approach (blue, see Table 2) to the currently employed clinical approach (gray) in terms of segmentation time, vessel tree construction time, control point addition, control point deletion, and

total time. We tested all data for normality (Shapiro-Wilk test, $p < 0.05$) and for significant differences between our and the routine approach (paired t -test, $p < 0.05$). We also calculated the mean and standard deviation, the difference in total time, and the performance factor. In terms of segmentation times, our approach was significantly faster ($p = 4.17e - 08$, on average 8:53 [mm:ss]) than the routine workflow in 22 of the 24 cases, except cases 4 and 13. There was no significant difference in the vessel tree construction times ($p = 0.08571$, on average 2:20 [mm:ss] faster), but our approach required significantly less interaction, i.e., control point additions ($p = 0.03417$, on average 13 less) and deletions ($p = 0.04625$, on average 2 less). As in the pilot study, the tracking was rarely undone in the clinical study (on average only once). This demonstrates that our proposed approach works as intended in clinical routine and can therefore be considered robust. Overall, our approach poses a substantial improvement, since it requires significantly

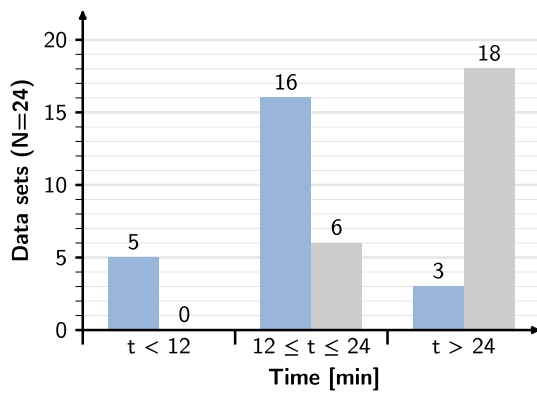


Fig. 9. Histogram of the required completion time of our proposed (blue) and the routine approach (gray). We selected three bins of 12 min each. Our approach required between 12 and 24 min for most data sets, while the routine approach usually required more than 24 min. (For interpretation of the references to colour in this figure legend, the reader is referred to the web version of this article.)

less user interaction and is considerably faster than the routine workflow ($17:24 \pm 6:44$ vs. $28:40 \pm 7:45$ [mm:ss]).

Fig. 9 shows the completion time histogram of our proposed (blue) and the routine approach (gray) using the clinical study data sets ($N = 24$), divided into the following three bins: $t < 12$ min, $12 \leq t \leq 24$ min, and $t > 24$ min. Most data sets ($N = 16$) belong to the central bin in our approach, while the employed approach usually ($N = 18$) requires more than 24 min per case. As mentioned by the evaluating radiologist, one possible reason for the difference in time distribution is that our proposed approach can track occluded vessels over longer distances, including their collateral vessels. This saves a lot of time because these vessels do not need to be defined manually, as in the routine approach. This clearly demonstrates that our proposed approach is a reasonable alternative to the current approach.

6. Conclusion and future work

We presented a method for segmenting and extracting the relevant vessels in peripheral CTA data sets. An innovative aspect of our approach is the tracking stage, in which the vessel tissue is propagated even if vessels touch bone or are disconnected. We evaluated our approach in two studies and received positive results, namely that it is not only accurate and efficient, but our approach is also robust, as it supports manual adjustments to improve unsatisfactory results. In contrast, available solutions often lack sufficient capabilities for manual corrections, rendering the produced reformations invalid for clinical analysis. Outside of dedicated cardiovascular centers, reading of peripheral CT angiographies is thus often still performed using only MPRs, which is not only time-consuming, but bears the risk of missing short, aperture-like lesions. Hence, our technique substantially improves the current workflow for the assessment of PAD. In difficult clinical cases, such as bypasses, metal artifacts, stents, and low contrast in the acquisition process, our collaborating physicians rated the outcome of our technique as positive, compared to the current clinical workflow, which is quite cumbersome and requires extensive user interaction and expertise. Our proposed approach solves these situations either automatically or with minimal user interaction. We believe that this is a particular strength for generating large, expert-annotated data sets required for the development of new machine learning algorithms. The large undiseased portions of the vessel tree are rapidly and efficiently extracted, allowing the expert supervisor to focus on the clinically important but often challenging diseased segments. The generation of high-quality, well curated databases is a major bottleneck for the development of the next generation AI/ML driven image processing

tools.

Nevertheless, there are two aspects to consider before our method can be incorporated into the daily clinical routine. If the linking does not lead to correct results, it might lead to a wrong overall vessel extraction [42]. We assume that physicians would feel more comfortable if the output of our algorithm could be confirmed after the linking before continuing. Physicians are sometimes also interested in the secondary arteries, e.g. the internal iliac arteries, in case the main ones are occluded. Our workflow allows them to detect the secondary arteries as well, but may require additional seed points, separation objects, or manual control point placements.

CRediT authorship contribution statement

Gabriel Mistelbauer: Conceptualization of evaluation, Methodology, Software, Writing – Original draft and final manuscript. Anca Morar: Conceptualization of evaluation, Methodology, Software, Writing – Original draft and final manuscript. Rüdiger Scherthaner: Data curation, Conceptualization and conduction of evaluation, Writing – Original draft. Andreas Strassl: Data curation, Conceptualization and conduction of evaluation, Writing – Original draft. Dominik Fleischmann: Writing – Original draft, Reviewing – Original draft and final manuscript. Florica Moldoveanu: Writing – Original draft, Reviewing – Original draft and final manuscript. M. Eduard Gröller: Writing – Original draft, Reviewing – Original draft and final manuscript.

Declaration of competing interest

The authors declare that they have no known competing financial interests or personal relationships that could have appeared to influence the work reported in this paper.

Acknowledgment

The clinical data were acquired at the General Hospital of Vienna, Austria, in a retrospective, ethical review board approved study (approval number: 1051/2017). Part of the research was facilitated by VRVis Research Center Austria, funded by COMET (879730), a program managed by the Austrian Research Promotion Agency (FFG).

References

- [1] V. Aboyans, J.B. Ricco, M.L.E.L. Bartelink, M. Björck, M. Brodmann, T. Cohnert, J. P. Collet, M. Czerny, M.D. Carlo, S. Debus, C. Espinola-Klein, T. Kahan, S. Kownator, L. Mazzolai, A.R. Naylor, M. Roffi, J. Röther, M. Sprynger, M. Tenders, G. Tepe, M. Venermo, C. Vlachopoulos, I. Desormais, Editor's choice – 2017 ESC guidelines on the diagnosis and treatment of peripheral arterial diseases, in collaboration with the European society for vascular surgery (ESVS), *Eur. J. Vasc. Endovasc. Surg.* 55 (2018) 305–368, <https://doi.org/10.1016/j.ejvs.2017.07.018>.
- [2] S. Aylward, S. Pizer, D. Eberly, E. Bullitt, Intensity ridge and widths for tubular object segmentation and description, in: *Proceedings of the Workshop on Mathematical Methods in Biomedical Image Analysis*, 1996, pp. 131–138.
- [3] S.R. Aylward, E. Bullitt, Initialization, noise, singularities, and scale in height ridge traversal for tubular object centerline extraction, *IEEE Trans. Med. Imag.* 21 (2002) 61–75.
- [4] F. Benmansour, L.D. Cohen, Tubular structure segmentation based on minimal path method and anisotropic enhancement, *Int. J. Comput. Vis.* 92 (2011) 192–210.
- [5] D.A. Borges Oliveira, L. Leal-Taixé, R. Queiroz Feitosa, B. Rosenhahn, Automatic tracking of vessel-like structures from a single starting point, *Comput. Med. Imag. Graph.* 47 (2016) 1–15, <https://doi.org/10.1016/j.compmedimag.2015.11.002>.
- [6] V. Bui, S.M. Shanbhag, O. Levine, M. Jacobs, W.P. Bandettini, L. Chang, M.Y. Chen, L. Hsu, Simultaneous multi-structure segmentation of the heart and peripheral tissues in contrast enhanced cardiac computed tomography angiography, *IEEE Access* 8 (2020) 16187–16202.
- [7] S. Cetin, A. Demir, A. Yezzi, M. Degertekin, G. Unal, Vessel tractography using an intensity based tensor model with branch detection, *IEEE Trans. Med. Imag.* 32 (2013) 248–363.
- [8] T.F. Chan, L.A. Vese, Active contours without edges, *IEEE Trans. Image Process.* 10 (2001) 266–277.
- [9] K. Chang, Y. Wu, W. Lin, S. Chen, L. Chen, Vessel segmentation based on bone-to-bone elimination in brain CT angiography, in: *Proceedings of IEEE International Conference on Consumer Electronics-Taiwan*, 2016, pp. 1–2.

- [10] S.M. Conte, P.R. Vale, Peripheral arterial disease, *Heart Lung Circ.* 27 (2018) 427–432, <https://doi.org/10.1016/j.hlc.2017.10.014>.
- [11] M. Freiman, N. Broide, M. Natanzon, E. Nammer, O. Shilon, L. Weizman, L. Joskowicz, J. Sosna, Vessels-cut: a graph based approach to patient-specific carotid arteries modeling, in: *Proceedings of the Conference on Modelling the Physiological Human*, 2009, pp. 1–12.
- [12] O. Friman, M. Hindennach, H. Peitgen, Template-based multiple hypotheses tracking of small vessels, in: *Proceedings of IEEE International Symposium on Biomedical Imaging: from Nano to Macro*, 2008, pp. 1047–1050.
- [13] M.A. Grölsün, G. Funke-Lea, Y. Zheng, M. Eckert, CTA coronary labeling through efficient geodesics between trees using anatomy priors, in: *Proceedings of International Conference on Medical Image Computing and Computer-Assisted Intervention*, 2014, pp. 521–528, https://doi.org/10.1007/978-3-319-10470-6_65.
- [14] Q. Hong, Q. Li, B. Wang, Y. Li, J. Yao, K. Liu, Q. Wu, 3D vasculature segmentation using localized hybrid level-set method, *Biomed. Eng. Online* 13 (2014).
- [15] X. Hu, D. Ding, Z. Li, Q. Ge, C. Jiang, J. Li, Z. Zhou, D. Chu, Axis-guided patch based accurate segmentation for pathological vessels using adaptive weight sparse representation, *Biomed. Signal Process Contr.* 57 (2020) 101817, <https://doi.org/10.1016/j.bspc.2019.101817>.
- [16] D. Jia, X. Zhuang, Directional fast-marching and multi-model strategy to extract coronary artery centerlines, *Comput. Biol. Med.* 108 (2019) 67–77, <https://doi.org/10.1016/j.compbiomed.2019.03.029>.
- [17] A. Kanitsar, R. Wegenkittl, P. Felkel, D. Fleischmann, D. Sandner, E. Gröller, Peripheral vessel investigation for routine clinical use, in: *Proceedings of IEEE Visualization*, 2001, pp. 477–480.
- [18] Y.M. Kassim, V.B.S. Prasath, O.V. Glinskii, V.V. Glinsky, V.H. Huxley, K. Palaniappan, Confocal vessel structure segmentation with optimized feature bank and random forests, in: *Proceedings of IEEE Applied Imagery Pattern Recognition Workshop*, 2016, <https://doi.org/10.1109/AIPR.2016.8010580>.
- [19] A. Kerkeni, A. Benabdallah, A. Manzanera, M.H. Bedoui, A coronary artery segmentation method based on multiscale area and region growing, *Comput. Med. Imag. Graph.* 48 (2016) 49–61, <https://doi.org/10.1016/j.compmedimag.2015.12.004>.
- [20] C. Kirbas, F. Quek, A review of vessel extraction techniques and algorithms, *ACM Comput. Surv.* 36 (2004) 81–121.
- [21] T.C. Lee, R.L. Kashyap, C.N. Chu, Building skeleton models via 3-d medial surface/axis thinning algorithms, *J. Graph. Model. Image Process.* 56 (1994) 464–478.
- [22] H. Li, A. Yezzi, Vessels as 4-d curves: global minimal 4-d paths to extract 3-d tubular surfaces and centerlines, *IEEE Trans. Med. Imag.* 26 (2007) 1213–1223.
- [23] K. Lidayova, H. Frimmel, E. Bengtsson, O. Smedby, Improved centerline tree detection of diseased peripheral arteries with a cascading algorithm for vascular segmentation, *Journal of Medical Imaging* 4 (2017), 024004, <https://doi.org/10.1117/1.JMI.4.2.024004>.
- [24] D. Major, A.A. Novikov, M. Wimmer, J. Hladuvka, K. Bühler, Automated slice-based artery identification in various field-of-view CTA scans, in: K. Bühler, L. Linsen, N.W. John (Eds.), *Proceedings of the Eurographics Workshop on Visual Computing for Biology and Medicine*, 2015, pp. 123–129.
- [25] D. Maksimov, F. Finkel, T. Dietz, S. Diehl, C. Duber, P. Rebholz, J. Hesser, R. Manner, An interactive application for removal of bone information in CT-angiography, in: *Proceedings of the IEEE Symposium on Computer-Based Medical Systems*, 2004, pp. 396–401.
- [26] D. Maksimov, J. Hesser, C. Brockmann, S. Jochum, T. Dietz, A. Schnitzer, C. Duber, S.O. Schoenberg, S. Diehl, Graph-matching based CTA, *IEEE Trans. Med. Imag.* 28 (2009) 1940–1954.
- [27] R. Manniesing, M.A. Viergever, W.J. Niessen, Vessel axis tracking using topology constrained surface evolution, *IEEE Trans. Med. Imag.* 26 (2007) 309–316.
- [28] P. Mirunalini, C. Aravindan, A.T. Nambi, S. Poorvaja, V.P. Priya, Segmentation of coronary arteries from CTA axial slices using deep learning techniques, in: *TENCON 2019 - 2019 IEEE Region 10 Conference (TENCON)*, 2019, pp. 2074–2080.
- [29] S. Moccia, E. De Momi, S. El Hadji, L.S. Mattos, Blood vessel segmentation algorithms — review of methods, datasets and evaluation metrics, *Comput. Methods Progr. Biomed.* 158 (2018) 71–91, <https://doi.org/10.1016/j.cmpb.2018.02.001>.
- [30] V. Mohan, G. Sundaramoorthi, A. Tannenbaum, Tubular surface segmentation for extracting anatomical structures from medical imagery, *IEEE Trans. Med. Imag.* 29 (2010) 1945–1958.
- [31] A. Morar, F. Moldoveanu, E. Gröller, Image segmentation based on active contours without edges, in: *Proceedings of the IEEE International Conference on Intelligent Computer Communication and Processing*, 2012, pp. 213–220.
- [32] R. Moreno, O. Smedby, Gradient-based enhancement of tubular structures in medical images, *Med. Image Anal.* 26 (2015) 19–29, <https://doi.org/10.1016/j.media.2015.07.001>.
- [33] S. Moriconi, M.A. Zuluaga, H.R. Jäger, P. Nachev, S. Ourselin, M.J. Cardoso, Inference of cerebrovascular topology with geodesic minimum spanning trees, *IEEE Trans. Med. Imag.* 38 (2019) 225–239, <https://doi.org/10.1109/TMI.2018.2860239>.
- [34] P. Nardelli, D. Jimenez-Carretero, D. Bermejo-Pelaez, G.R. Washko, F.N. Rahaghi, M.J. Ledesma-Carbayo, R.S.J. Estépar, Pulmonary artery–vein classification in CT images using deep learning, *IEEE Trans. Med. Imag.* 37 (2018) 2428–2440.
- [35] L. Norgren, W.R. Hiatt, J.A. Dormandy, M.R. Nehler, K.A. Harris, F.G.R. Fowkes, Inter-society consensus for the management of peripheral arterial disease (TASC II), *J. Vasc. Surg.* 45 (2007) S5–S67, <https://doi.org/10.1016/j.jvs.2006.12.037>.
- [36] A. Novikov, D. Major, M. Wimmer, G. Sluiter, K. Bühler, Automated anatomy-based tracking of systemic arteries in arbitrary field-of-view CTA scans, *IEEE Trans. Med. Imag.* 36 (2017) 1359–1371.
- [37] S.D. Olabarriaga, M. Breeuwer, W.J. Niessen, Minimum cost path algorithm for coronary artery central axis tracking in CT images, in: R.E. Ellis, T.M. Peters (Eds.), *Proceedings of the Conference on Medical Image Computing and Computer-Assisted Intervention*, 2003, pp. 687–694, https://doi.org/10.1007/978-3-540-39903-2_84.
- [38] T. Pock, R. Beichel, H. Bischof, A novel robust tube detection filter for 3D centerline extraction, in: *Proceedings of the Conference on Image Analysis*, 2005, pp. 481–490.
- [39] J. Roos, D. Fleischmann, K. A. T. Rakshe, M. Straka, A. Napoli, A. Kanitsar, M. Sramek, E. Gröller, Multipath curved planar reformation of the peripheral arterial tree in CT angiography, *Radiology* 224 (2007) 281–290.
- [40] P. Sanches, C. Meyer, V. Vigon, B. Naegel, Cerebrovascular network segmentation of MRA images with deep learning, in: *Proceedings of IEEE International Symposium on Biomedical Imaging*, 2019, pp. 768–771.
- [41] N. Sangsefidi, A.H. Foruzan, A. Dolati, Balancing the data term of graph-cuts algorithm to improve segmentation of hepatic vascular structures, *Comput. Biol. Med.* 93 (2018) 117–126, <https://doi.org/10.1016/j.compbiomed.2017.12.019>.
- [42] M.M. Schreiner, H. Platzgummer, S. Unterhumer, M. Weber, G. Mistelbauer, E. Gröller, C. Loewe, R.E. Scherthaner, Multipath curved planar reformations of peripheral CT angiography: diagnostic accuracy and time efficiency, *Cardiovasc. Intervent. Radiol.* 41 (2018) 718–725, <https://doi.org/10.1007/s00270-017-1846-3>.
- [43] R. Selvan, J. Petersen, J.H. Pedersen, M. de Bruijne, Extracting tree structures in CT data by tracking multiple statistically ranked hypotheses, *Med. Phys.* 46 (2019) 4431–4440, <https://doi.org/10.1002/mp.13711>.
- [44] R. Shahzad, O. Dzyubachyka, M. Staringa, J. Kullberg, L. Johansson, H. Ahlström, B.P. Lelieveldt, R.J. van der Geest, Automated extraction and labelling of the arterial tree from whole-body MRA data, *Med. Image Anal.* 24 (2015) 28–40.
- [45] F. Shi, Q. Yang, X. Guo, T.A. Qureshi, Z. Tian, H. Miao, D. Dey, D. Li, Z. Fan, Intracranial vessel wall segmentation using convolutional neural networks, *IEEE (Inst. Electr. Electron. Eng.) Trans. Biomed. Eng.* 66 (2019) 2840–2847.
- [46] H. Shim, D. Kwon, I.D. Yun, S.U. Lee, Robust segmentation of cerebral arterial segments by a sequential Monte Carlo method: particle filtering, *Comput. Methods Progr. Biomed.* 84 (2006) 135–145.
- [47] R.C. Sibley, S.P. Reis, J.J. MacFarlane, M.A. Reddick, S.P. Kalva, P.D. Sutphin, Radiographics. Noninvasive Physiologic Vascular Studies: A Guide to Diagnosing Peripheral Arterial Disease 37 (2017) 346–357, <https://doi.org/10.1148/rq.2017160044>.
- [48] P. Song, D. Rudan, Y. Zhu, F.J.I. Fowkes, K. Rahimi, F.G.R. Fowkes, I. Rudan, Global, regional, and national prevalence and risk factors for peripheral artery disease in 2015: an updated systematic review and analysis, *The Lancet Global Health* 7 (2019) e1020–e1030, [https://doi.org/10.1016/S2214-109X\(19\)30255-4](https://doi.org/10.1016/S2214-109X(19)30255-4).
- [49] T.A. Soomro, A.J. Afifi, L. Zheng, S. Soomro, J. Gao, O. Hellwich, M. Paul, Deep learning models for retinal blood vessels segmentation: a review, *IEEE Access* 7 (2019) 71696–71717.
- [50] M. Straka, Processing and Visualization of Peripheral CT-Angiography Datasets, Ph.D. thesis. TU Wien, Vienna, Austria, 2006.
- [51] S. Tabik, E.M. Garzon, I. Garcia, J.J. Fernandez, Implementation of anisotropic nonlinear diffusion for filtering 3D images in structural biology on smp clusters, in: *Proceedings of the Conference on Parallel Computing: Current & Future Issues of High-End Computing*, 2005, pp. 727–734.
- [52] I.A. Tache, Vessels enhancement in x-ray angiograms, in: *Proceedings of E-Health and Bioengineering Conference*, 2015, pp. 1–4.
- [53] I.A. Tache, Vessel segmentation of coronary x-ray angiograms, in: *Proceedings of International Conference on System Theory, Control and Computing*, 2016, pp. 727–731.
- [54] R. Tanaka, K. Yoshioka, H. Takagi, J.D. Schuijff, K. Arakita, Novel developments in non-invasive imaging of peripheral arterial disease with CT: experience with state-of-the-art, ultra-high-resolution CT and subtraction imaging, *Clin. Radiol.* 74 (2019) 51–58, <https://doi.org/10.1016/j.crad.2018.03.002>.
- [55] G. Tetteh, V. Efremov, N.D. Forkort, M. Schneider, J. Kirschke, B. Weber, C. Zimmer, M. Piraud, B. Menze, DeepVesselNet: vessel segmentation, centerline prediction, and bifurcation detection in 3-D angiographic volumes, *Front. Neurosci.* 14 (2020) 1–17, <https://doi.org/10.3389/fnins.2020.592352>.
- [56] M.I. Todorov, J.C. Paetzold, O. Schoppe, G. Tetteh, S. Shit, V. Efremov, K. Todorov-Völgyi, M. Düring, M. Dichgans, M. Piraud, B. Menze, A. Ertürk, Machine learning analysis of whole mouse brain vasculature, *Nat. Methods* 17 (2020) 442–449, <https://doi.org/10.1038/s41592-020-0792-1>.
- [57] B.D. de Vos, J.M. Wolterink, P.A. de Jong, T. Leiner, M.A. Viergever, I. Išgum, Convnet-based localization of anatomical structures in 3-d medical images, *IEEE Trans. Med. Imag.* 36 (2017) 1470–1481.
- [58] C. Wang, O. Smedby, Coronary artery segmentation and skeletonization based on competing fuzzy connectedness tree, in: *Proceedings of the Conference on Medical Image Computing and Computer-Assisted Intervention*, 2007, pp. 311–318.
- [59] Y. Wang, J. Chen, C. Liu, Z. Mao, Stacked fully convolutional networks for pulmonary vessel segmentation, in: *Proceedings of IEEE Visual Communications and Image Processing*, 2018, pp. 1–4.
- [60] J. Weickert, Anisotropic Diffusion in Image Processing, 1998. B.G. Teubner (Stuttgart).
- [61] J.M. Wolterink, R.W. van Hamersvelt, M.A. Viergever, T. Leiner, I. Išgum, Coronary artery centerline extraction in cardiac CT angiography using a CNN-based orientation classifier, *Med. Image Anal.* 51 (2019) 46–60, <https://doi.org/10.1016/j.media.2018.10.005>.

- [62] A. Wu, Z. Xu, M. Gao, M. Buty, D.J. Mollura, Deep vessel tracking: a generalized probabilistic approach via deep learning, in: *Proceedings of International Symposium on Biomedical Imaging*, 2016, pp. 1363–1367.
- [63] M. Xie, Y. Li, Y. Xue, R. Shafritz, S.A. Rahimi, J.W. Ady, U.W. Roshan, Vessel lumen segmentation in internal carotid artery ultrasounds with deep convolutional neural networks, in: *Proceedings of IEEE International Conference on Bioinformatics and Biomedicine, BIBM*, 2019, pp. 2393–2398, <https://doi.org/10.1109/BIBM47256.2019.8982980>.
- [64] L. Yuan, L. Zhang, H. Ditt, V. Ordy, F. Pereira, C. Chefid'hotel, Simultaneous label fusion with vessel preserving for bone removal in CT angiography scans, in: *Proceedings of IEEE Engineering in Medicine and Biology Society*, 2013, pp. 5115–5118, <https://doi.org/10.1109/EMBC.2013.6610699>.
- [65] S. Zhao, X. Wang, Y. Tian, Q. Deng, Z. Wu, M. Zhou, Gap connection of vascular branches by nonlinear least squares curve fitting algorithm, in: *Proceedings of ACM SIGGRAPH Conference on Virtual-Reality Continuum and its Applications in Industry*, 2016, pp. 345–352, <https://doi.org/10.1145/3013971.3015778>.
- [66] W. Zhao, H. He, J. Zhao, J. Sun, Adrenal tumor vessels segmentation using convolutional neural network in computed tomography angiography, in: *Proceedings of IEEE Engineering in Medicine and Biology Society*, 2019, pp. 1006–1009.
- [67] M. Zreik, R.W. van Hamersvelt, N. Khalili, J.M. Wolterink, M. Voskuil, M. A. Viergever, T. Leiner, I. Išgum, Deep learning analysis of coronary arteries in cardiac CT angiography for detection of patients requiring invasive coronary angiography, *IEEE Trans. Med. Imag.* 39 (2020) 1545–1557, <https://doi.org/10.1109/TMI.2019.2953054>.
- [68] M. Zreik, R.W. van Hamersvelt, J.M. Wolterink, T. Leiner, M.A. Viergever, I. Išgum, A recurrent CNN for automatic detection and classification of coronary artery plaque and stenosis in coronary CT angiography, *IEEE Trans. Med. Imag.* 38 (2019) 1588–1598, <https://doi.org/10.1109/TMI.2018.2883807>.



Andreas Strassl is a radiology technologist working as a scientific assistant for the Department of Biomedical Imaging and Image-Guided Therapy, Medical University of Vienna. He received a Master's degree in functional imaging, conventional and ion radiotherapy in 2020. His research interests include morphological as well as functional imaging, image post-processing and radiomics, predominantly in the field of computed tomography.



Dominik Fleischmann is professor of radiology with the Stanford University School of Medicine, CA. He is the chief of cardiovascular imaging in the Department of Radiology since 2011, and the director of computed tomography with Stanford Hospital and Clinics since 2008, and medical director of the Stanford 3DQ Imaging Laboratory since 2012. His work focuses on cardiovascular imaging and image analysis.



Gabriel Mistelbauer is a postdoctoral researcher at the Otto-von-Guericke University Magdeburg, Germany since 2016. Previously, he was a postdoctoral researcher at TU Wien, Austria, where he received his PhD in computer science in the field of medical visualization in 2013. His research focuses on visual computing in medicine and medical image processing, but in particular on the analysis of vascular structures.



Florica Moldoveanu is professor at University POLITEHNICA of Bucharest and responsible for two master programs: Management in Information Technology and Computer Graphics, Multimedia and Virtual Reality. Her research is focused on computer graphics, image processing and e-health. She is the president of the Health Level 7 Romania Association.



Anca Morar is an associate professor at University POLITEHNICA of Bucharest, Romania since 2018. She received her Ph.D. (2012) in computer science in the field of medical image analysis and visualization. Her research is focused on computer graphics, GPGPU, computer vision and e-health.



M. Eduard Gröller is professor at TU Wien, Austria, and adjunct professor of computer science at the University of Bergen, Norway. His research interests include computer graphics, visualization and visual computing. He is heading the research unit of Computer Graphics at TU Wien and is a key researcher at the VRVis Research Center.



Rüdiger Scherthaner is an Associate Professor of Radiology at the Medical University of Vienna, Austria. From 2013 to 2015, he was a Visiting Scientist at the Johns Hopkins University, Baltimore, MD, USA. Since 2021, he is head of the department of Radiology at the Hospital Landstrasse in Vienna, Austria. His research interests are cardiovascular imaging and interventional oncology.